First simultaneous measurement of sextupolar and octupolar resonance driving terms in a circular accelerator from turn-by-turn beam position monitor data

A. Franchi,* L. Farvacque, F. Ewald, G. Le Bec, and K. B. Scheidt

ESRF, CS 40220, 38043 Grenoble Cedex 9, France

(Received 7 February 2014; published 8 July 2014)

Beam lifetime in storage rings and colliders is affected by, among other effects, lattice nonlinearities. Their control is of great benefit to the dynamic aperture of an accelerator, whose enlargement leads in general to more efficient injection and longer lifetime. This article describes a procedure to evaluate and correct unwanted nonlinearities by using turn-by-turn beam position monitor data, which is an evolution of previous works on the resonance driving terms (RDTs). Effective normal and skew sextupole magnetic errors at the ESRF electron storage ring are evaluated and corrected (when possible) by using this technique. For the first time, also octupolar RDTs could be measured and used to define an octupolar model for the main quadrupoles. Most of the deviations from the model observed in the sextupolar RDTs of the ESRF storage ring turned out to be generated by focusing errors rather than by sextupole errors. These results could be achieved thanks to new analytical formulas describing the harmonic content of the nonlinear betatron motion to the second order. For the first time, linear combinations of RDTs have been also used for beam-based calibration of individual sextupole magnets. They also proved to be a powerful tool in predicting faulty magnets and in validating magnetic models. This technique also provides a figure of merit for a self-assessment of the reliability of the data analysis.

DOI: 10.1103/PhysRevSTAB.17.074001 PACS numbers: 29.20.-c

I. INTRODUCTION AND MOTIVATION

Many factors make the implementation of a magnetic optics in a circular accelerator different from the nominal one, among which are: deviations from the magnet calibration curves and from the ideal magnetic lengths, displacements from the reference position and axis, and unknown multipole components. This generally results in machine performances below expectations: low beam lifetime and dynamic aperture, poor injection efficiency, large emittances (in lepton machines), and limited luminosity (in colliders).

While an artillery of different methods and algorithms has been developed and successfully implemented in routine operation for the evaluation and correction of focusing errors (linear optics) and betatron coupling, their extension to the nonlinear modeling and correction remains difficult because they are either time-consuming or require diagnostic tools unavailable a decade ago. In most cases, such as at the ESRF storage ring, the correction of the nonlinear optics is done by trial and error seeking heuristically longer lifetime. Nevertheless, the installation of beam position monitors (BPMs) with turn-by-turn (TbT) acquisition system in many circular accelerators and the parallel development of a theoretical formalism for the description of the harmonic content of the acquired data paved the way for more rapid and deterministic measurement and correction of the nonlinear optics. This paper proposes a new method aiming at such characteristics.

Several approaches for the evaluation of the nonlinear lattice model exist and any attempt to offer a coverage of the pertinent literature would be incomplete. However, in the context of this paper a few works may be recalled, either for their proximity or because they represented milestones for this work. A pioneering work on the exploitation of TbT BPM data dates back to the early 1990s [1]. The application of the normal form approach [2,3] to single-particle tracking data of Ref. [4] introduced for the first time an explicit correspondence between spectral lines of TbT data and resonance driving terms (RDTs). A breakthrough was represented by the experience at the CERN Super Proton Synchrotron, where sextupolar RDTs along the entire ring were measured and used to detect faulty sextupole magnets [5] and to extract strength and polarity of some sextupoles [6,7]. More recently independent component analysis (ICA) was applied to TbT BPM data for the extraction of lattice linear and nonlinear properties [8]. Of interest are also the experimental results of Ref. [9], where the nonlinear model was fit to the spectral content of TbT data, even though not via the RDTs. In Refs. [10,11] simultaneous measurements of two RDTs, one sextupolar and one octupolar, are reported.

*andrea.franchi@esrf.fr

The paper is structured as follows. After highlighting and anticipating both advantages and limitations of the proposed method in Sec. I, the technique is introduced and discussed in its main results in Sec. III. The experimental results of the new method in evaluating the nonlinear model, calibrating sextupole magnets, and computing a corrector setting are presented in Sec. IV. The analysis of octupolar terms is described in Sec. V. Mathematical derivations are summarized in separate appendices (complete proofs may be found in Ref. [12]).

II. HIGHLIGHTS AND LIMITATIONS OF THE PROPOSED METHOD

The main highlights of the proposed scheme may be listed as follows: (i) The harmonic analysis is performed on the pure position data x (y), rather than on the complex signal $x - ip_x$ ($y - ip_y$) of Refs. [4,5], hence with no concern about errors in the evaluation of the momentum p_x (p_y) and about BPM synchronization; (ii) The possibility of measuring at the same time linear combinations of all sextupolar (normal and skew) and most of octupolar RDTs offers a complete and simultaneous picture of all resonances at a given working point, rather than having to shift the tunes close to a single resonant condition to excite a specific mode, as in Ref. [8]; (iii) The nonlinear problem of inferring sextupole and octupole strengths from the betatron beam motion is translated into a linear system to be inverted (with due preliminary precautions) when RDTs are used as observables, hence rendering the model fit and correction straightforward; (iv) Last but not least, the quality of the analysis of sextupolar RDTs may be self-assessed, so as to optimize the experimental conditions as well as the initial lattice model.

Of course, this approach suffers from some practical limitations too.

First, the quality of the analysis is limited by the spectral resolution, here defined as the ratio between the amplitudes of the harmonics and the background noise. The resolution scales with the number of turns of acquired data exploitable for a fast Fourier transform (FFT). Ideally, the greater the number of turns with exploitable data, the higher the spectral resolution and hence the quality of the RDT measurement. Data filtering and interpolation [13,14] may provide excellent resolution already with tens of turns, though the presence of noise [15] and the need of detecting spectral lines whose amplitudes are orders of magnitude lower than the tune line necessitate several hundreds of exploitable oscillation turns. Chromaticity and decoherence (induced by nonzero amplitude dependent detuning) modulate and damp the TbT signal [16]. This multiparticle effect is not contemplated here, the baseline model being of a beam moving rigidly as a single particle. Most of the operational settings optimized for beam lifetime and stability result in nonzero chromaticity and amplitude dependent detuning. In the case of the ESRF storage ring, the exploitable number of turns ranges from about 30 to 60 turns, depending on the optics put in operation, insufficient to detect sextupolar harmonics whose amplitude is typically 2 or 3 orders of magnitude lower than the tune line. Therefore, a special optics was designed to provide almost zero linear chromaticity and detuning. For hadron machines this may be sufficient to obtain thousands of exploitable TbT data, as in Ref. [8]. In lepton machines radiation damping depresses naturally the TbT signal. At the ESRF storage ring, the damping time being of about 2500 turns, the signal is sufficiently depressed to compromise the whole measurement already after 1024 turns (see Fig. 1) resulting in larger spectral background noise, as displayed in Fig. 2. Usually either 256 or 512 turns are used for the FFT, as radiation damping would enhance the background spectral noise.

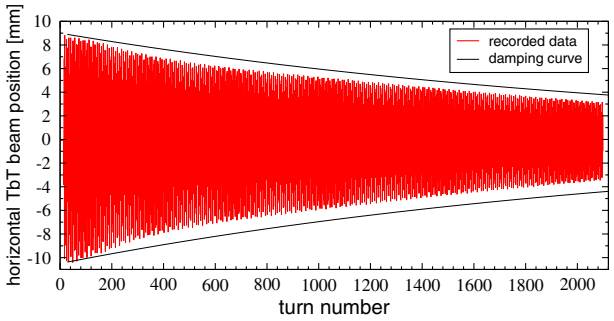

FIG. 1. Example of horizontal turn-by-turn beam oscillation after the pulse of an horizontal kicker magnet measured at the ESRF electron storage ring. A special sextupole setting was used to minimize amplitude dependent detuning and chromaticity. The decreasing amplitude is believed to be the result of radiation damping (black curve, damping time of 7 ms, corresponding to about 2500 turns).

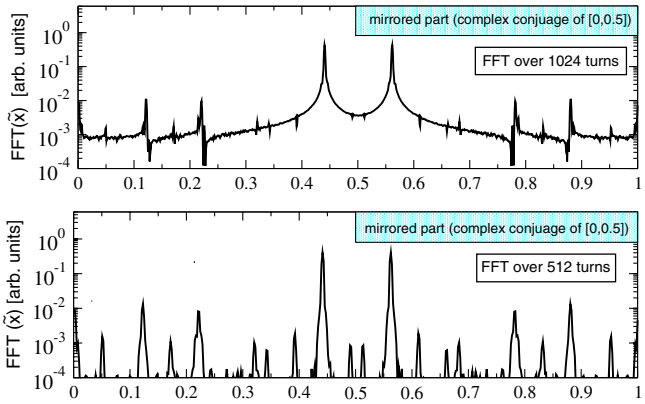

FIG. 2. Example of horizontal turn-by-turn spectra measured at the ESRF electron storage ring. The two plots are the FFT of the real signal $\tilde{x}(N) = x(N)/\sqrt{\beta_x}$ computed over 1024 and 512 turns, respectively. Despite the longer signal, the spectrum with 1024 turns shows higher background noise, which is attributed to radiation damping. In both cases, the region [0.5,1] is the mirrored copy (i.e., complex conjugate) of the region [0,0.5].

Second in the list of limitations is the BPM electronic resolution and noise. The commercial Libera Brilliance [17] BPMs installed in the ESRF storage ring are equipped with a standard electronic filter that covers several turns, resulting in TbT data corrupted from the neighbor turns. Even though a convolution may be carried out to extract clean TbT data, the spectral resolution remained insufficient for a detailed nonlinear analysis. A great improvement was achieved when implementing a moving-average filter (MAF) [18]. All results presented here are based on acquisitions carried out with this filter.

A last limitation is linked to the linear system to be pseudoinverted to extract the nonlinear model. The singular value decomposition (SVD) has been used for this purpose. The resulting model shall be then considered as effective and the inferred sextupole errors depend clearly on the numerical parameters (such as number of eigenvectors, choice of weights among different possible sources of errors).

III. COMBINED RESONANCE DRIVING TERMS FROM (DUAL-PLANE) BPM DATA

A. Theoretical results

In this section the correlation between the harmonic content of an *ideal* TbT oscillation in the two transverse planes, x and y, and the RDTs is discussed. For *ideal* it is meant here a free oscillation of an instantaneously displaced particle beam without any damping (for instance from radiation, chromaticity, amplitude dependent detuning) and with perfectly calibrated BPMs. Forced oscillations induced by resonant devices, such as AC dipoles, require a different description [19,20].

In Table I the spectral lines of the signals $\tilde{x}(N) = x(N)/\sqrt{\beta_x}$ and $\tilde{y}(N) = y(N)/\sqrt{\beta_y}$, where β denotes the Courant-Snyder (C-S) parameter, are listed together with the corresponding RDTs. Higher-order octupolar lines are analyzed in Sec. V. For the evaluation of the RDTs the complete phase space curve (x, p_x) and (y, p_y) generated by the TbT oscillation is necessary, which in turn requires the combination of signals from 2 synchronized BPMs. By analyzing its projection on the x and y axis, i.e., by using single-BPM TbT data, RDTs are no longer measurable. However, their linear combinations, the combined RDTs (CRDTs) F_{xy}, F_{yx}, F_{NS}, and F_{SS} are still observables. CRDTs are defined in the fourth column of Table I and are derived in Appendix C. In Table II formulas to infer their amplitudes and phases from the spectral lines are reported, whereas analytic formulas for the computation of first-order RDTs, and hence of the CRDTs, from the lattice model are listed in Table III.

Before entering in the perilous terrain of higher orders, it is worthwhile to define what actually *order* means. As opposed to Ref. [2], the distance from the origin, i.e., the invariant, is not used here as a perturbative parameter defining the order of the analysis. In Appendix A it is shown how the nonlinear betatron motion may be described in terms of truncated Lie series: the degree of precision (and difficulty) of the description is related to the order at which

TABLE I. List of lines in the spectra of $\tilde{x}(N)$ and $\tilde{y}(N)$ with corresponding measurable combined RDTs (CRDTs) $F = |F|e^{iq_F}$ and excited resonances. A horizontal (vertical) spectral line $H(n_x, n_y)$ $[V(n_x, n_y)]$ is located at the frequency $n_x Q_x + n_y Q_y$. For each line, expressions for its amplitude and phase are given. The choice was made here to make use of the lines in the region [0,0.5] in tune units, and both tunes are assumed to lay in that interval. First-order RDTs (defined in Table III) are sufficient for coupling and normal sextupoles, while the analysis of skew sextupole terms requires a second-order analysis, through the observable RDTs (ORDTs) g_{jklm} of Table XIV (The justification for such a choice is given in Appendix B). Quadrupole errors are to be included in the model when computing the Courant-Snyder (C-S) parameters used to evaluate $\tilde{x}(N)$, $\tilde{y}(N)$ and the RDTs $f^{(1)}_{jklm}$ of Table III.

Spectral line	Amplitude	Phase ϕ	Combined RDT	Resonances	Magnetic term
$H(1,0)$	$\frac{1}{2}(2I_x)^{1/2}$	ψ_{x0}			Normal quadrupole
$V(0,1)$	$\frac{1}{2}(2I_y)^{1/2}$	ψ_{y0}			Normal quadrupole
$H(0,1)$	$(2I_y)^{1/2}\lvert F_{xy}\rvert$	$q_{F_{xy}} + \frac{3}{2}\pi + \psi_{y0}$	$F_{xy} = f^{(1)}_{1001} - f^{(1)*}_{1010}$	$(1,1),(1,-1)$	Skew quadrupole
$V(1,0)$	$(2I_x)^{1/2}\lvert F_{yx}\rvert$	$q_{F_{yx}} + \frac{3}{2}\pi + \psi_{x0}$	$F_{yx} = f^{(1)*}_{1001} - f^{(1)*}_{1010}$	$(1,1),(1,-1)$	Skew quadrupole
$H(-2,0)$	$(2I_x)\lvert F_{NS3}\rvert$	$q_{F_{NS3}} + \frac{3}{2}\pi - 2\psi_{x0}$	$F_{NS3} = 3f^{(1)}_{3000} - f^{(1)*}_{1200}$	(1,0),(3,0)	Normal sextupole
$H(0,-2)$	$(2I_y)\lvert F_{NS2}\rvert$	$q_{F_{NS2}} + \frac{3}{2}\pi - 2\psi_{y0}$	$F_{NS2} = f^{(1)}_{1020} - f^{(1)}_{0120}$	$(1,-2),(1,2)$	Normal sextupole
$V(-1,-1)$	$(2I_x 2I_y)^{1/2}\lvert F_{NS1}\rvert$	$q_{F_{NS1}} + \frac{3}{2}\pi - \psi_{x0} - \psi_{y0}$	$F_{NS1} = 2f^{(1)}_{1020} - f^{(1)*}_{0111}$	$(1,2),(1,0)$	Normal sextupole
$V(1,-1)$	$(2I_x 2I_y)^{1/2}\lvert F_{NS0}\rvert$	$q_{F_{NS0}} + \frac{3}{2}\pi + \psi_{x0} - \psi_{y0}$	$F_{NS0} = 2f^{(1)}_{0120} - f^{(1)}_{0111}$	$(1,-2),(1,0)$	Normal sextupole
$V(0,-2)$	$(2I_y)\lvert F_{SS3}\rvert$	$q_{F_{SS3}} + \frac{3}{2}\pi - 2\psi_{y0}$	$F_{SS3} = 3g_{0030} - g^{*}_{0012}$	(0,1),(0,3)	Skew sextupole
$V(-2,0)$	$(2I_x)\lvert F_{SS2}\rvert$	$q_{F_{SS2}} + \frac{3}{2}\pi - 2\psi_{x0}$	$F_{SS2} = g_{2010,V} - g^{*}_{0210}$	$(2,-1),(2,1)$	Skew sextupole
$H(-1,-1)$	$(2I_x 2I_y)^{1/2}\lvert F_{SS1}\rvert$	$q_{F_{SS1}} + \frac{3}{2}\pi - \psi_{x0} - \psi_{y0}$	$F_{SS1} = 2g_{2010,H} - g^{*}_{1101}$	$(2,-1),(0,1)$	Skew sextupole
$H(1,-1)$	$(2I_x 2I_y)^{1/2}\lvert F_{SS0}\rvert$	$q_{F_{SS0}} + \frac{3}{2}\pi + \psi_{x0} - \psi_{y0}$	$F_{SS0} = g_{1110} - 2g^{*}_{2001}$	$(2,-1),(0,1)$	Skew sextupole

TABLE II. Formulas to evaluate combined RDTs (CRDTs) from the secondary lines in the spectra of $\tilde{x}(N)$ and $\tilde{y}(N)$ assuming properly calibrated BPMs, turn-by-turn oscillations without decoherence and quadrupole errors included in the C-S parameters.

Combined RDT	Amplitude	Phase q_F
$F_{xy} = \lvert F_{xy}\rvert e^{iq_{F_{xy}}}$	$\lvert F_{xy}\rvert = \lvert H(0,1)\rvert/[2\lvert V(0,1)\rvert]$	$q_{F_{xy}} = \phi_{H(0,1)} - \phi_{V(0,1)} - \frac{3}{2}\pi$
$F_{yx} = \lvert F_{yx}\rvert e^{iq_{F_{yx}}}$	$\lvert F_{yx}\rvert = \lvert V(1,0)\rvert/[2\lvert H(1,0)\rvert]$	$q_{F_{yx}} = \phi_{V(1,0)} - \phi_{H(1,0)} - \frac{3}{2}\pi$
$F_{NS3} = \lvert F_{NS3}\rvert e^{iq_{F_{NS3}}}$	$\lvert F_{NS3}\rvert = \lvert H(-2,0)\rvert/[4\lvert H(1,0)\rvert^2]$	$q_{F_{NS3}} = \phi_{H(-2,0)} + 2\phi_{H(1,0)} - \frac{3}{2}\pi$
$F_{NS2} = \lvert F_{NS2}\rvert e^{iq_{F_{NS2}}}$	$\lvert F_{NS2}\rvert = \lvert H(0,-2)\rvert/[4\lvert V(0,1)\rvert^2]$	$q_{F_{NS2}} = \phi_{H(0,-2)} + 2\phi_{V(0,1)} - \frac{3}{2}\pi$
$F_{NS1} = \lvert F_{NS1}\rvert e^{iq_{F_{NS1}}}$	$\lvert F_{NS1}\rvert = \lvert V(-1,-1)\rvert/[4\lvert H(1,0)\rvert\lvert V(0,1)\rvert]$	$q_{F_{NS1}} = \phi_{V(-1,-1)} + \phi_{H(1,0)} + \phi_{V(0,1)} - \frac{3}{2}\pi$
$F_{NS0} = \lvert F_{NS0}\rvert e^{iq_{F_{NS0}}}$	$\lvert F_{NS0}\rvert = \lvert V(1,-1)\rvert/[4\lvert H(1,0)\rvert\lvert V(0,1)\rvert]$	$q_{F_{NS0}} = \phi_{V(1,-1)} - \phi_{H(1,0)} + \phi_{V(0,1)} - \frac{3}{2}\pi$
$F_{SS3} = \lvert F_{SS3}\rvert e^{iq_{F_{SS3}}}$	$\lvert F_{SS3}\rvert = \lvert V(0,-2)\rvert/[4\lvert V(0,1)\rvert^2]$	$q_{F_{SS3}} = \phi_{V(0,-2)} + 2\phi_{V(0,1)} - \frac{3}{2}\pi$
$F_{SS2} = \lvert F_{SS2}\rvert e^{iq_{F_{SS2}}}$	$\lvert F_{SS2}\rvert = \lvert V(-2,0)\rvert/[4\lvert H(1,0)\rvert^2]$	$q_{F_{SS2}} = \phi_{V(-2,0)} + 2\phi_{H(1,0)} - \frac{3}{2}\pi$
$F_{SS1} = \lvert F_{SS1}\rvert e^{iq_{F_{SS1}}}$	$\lvert F_{SS1}\rvert = \lvert H(-1,-1)\rvert/[4\lvert H(1,0)\rvert\lvert V(0,1)\rvert]$	$q_{F_{SS1}} = \phi_{H(-1,-1)} + \phi_{H(1,0)} + \phi_{V(0,1)} - \frac{3}{2}\pi$
$F_{SS0} = \lvert F_{SS0}\rvert e^{iq_{F_{SS0}}}$	$\lvert F_{SS0}\rvert = \lvert H(1,-1)\rvert/[4\lvert H(1,0)\rvert\lvert V(0,1)\rvert]$	$q_{F_{SS0}} = \phi_{H(1,-1)} - \phi_{H(1,0)} + \phi_{V(0,1)} - \frac{3}{2}\pi$

TABLE III. Formulas to calculate first-order RDTs from the lattice model. The magnet integrated strengths (MADX definition) are J_1 (m^{-1}), K_2, and J_2 (m^{-2}) for skew quadrupoles, normal, and skew sextupoles, respectively. The C-S parameters β and ϕ are evaluated from the linear lattice model with quadrupole errors (i.e., beta-beating) included. $\Delta\phi_w$ is the phase advance between the magnet w and the location where the RDTs are computed (BPM). $Q_{x,y}$, denote the linear betatron tunes, or eigentunes if coupling may not be neglected [21].

RDT	Resonance and magnetic term
$f^{(1)}_{1001} = \frac{\sum_w J_{w,1}\sqrt{\beta_x^w\beta_y^w}e^{i(\Delta\phi_{w,x}-\Delta\phi_{w,y})}}{4[1-e^{2\pi i(Q_x-Q_y)}]}$	(1,−1) skew quadrupole
$f^{(1)}_{1010} = \frac{\sum_w J_{w,1}\sqrt{\beta_x^w\beta_y^w}e^{i(\Delta\phi_{w,x}+\Delta\phi_{w,y})}}{4[1-e^{2\pi i(Q_x+Q_y)}]}$	(1, 1) skew quadrupole
$f^{(1)}_{3000} = -\frac{\sum_w K_{w,2}(\beta_x^w)^{3/2}e^{i(3\Delta\phi_{w,x})}}{48[1-e^{2\pi i(3Q_x)}]}$	(3,0) normal sextupole
$f^{(1)}_{1200} = -\frac{\sum_w K_{w,2}(\beta_x^w)^{3/2}e^{i(-\Delta\phi_{w,x})}}{16[1-e^{2\pi i(-Q_x)}]}$	(1,0) normal sextupole
$f^{(1)}_{1020} = \frac{\sum_w K_{w,2}\sqrt{\beta_x^w\beta_y^w}e^{i(\Delta\phi_{w,x}+2\Delta\phi_{w,y})}}{16[1-e^{2\pi i(Q_x+2Q_y)}]}$	(1,2) normal sextupole
$f^{(1)}_{0120} = \frac{\sum_w K_{w,2}\sqrt{\beta_x^w\beta_y^w}e^{i(-\Delta\phi_{w,x}+2\Delta\phi_{w,y})}}{16[1-e^{2\pi i(-Q_x+2Q_y)}]}$	(1,−2) normal sextupole
$f^{(1)}_{0111} = \frac{\sum_w K_{w,2}\sqrt{\beta_x^w\beta_y^w}e^{i(-\Delta\phi_{w,x})}}{8[1-e^{2\pi i(-Q_x)}]}$	(1,0) normal sextupole
$f^{(1)}_{0030} = -\frac{\sum_w J_{w,2}(\beta_y^w)^{3/2}e^{i(3\Delta\phi_{w,y})}}{48[1-e^{2\pi i(3Q_y)}]}$	(0,3) skew sextupole
$f^{(1)}_{0012} = -\frac{\sum_w J_{w,2}(\beta_y^w)^{3/2}e^{i(-\Delta\phi_{w,y})}}{16[1-e^{2\pi i(-Q_y)}]}$	(0,1) skew sextupole
$f^{(1)}_{2010} = \frac{\sum_w J_{w,2}\beta_x^w\sqrt{\beta_y^w}e^{i(2\Delta\phi_{w,x}+\Delta\phi_{w,y})}}{16[1-e^{2\pi i(2Q_x+Q_y)}]}$	(2,1) skew sextupole
$f^{(1)}_{2001} = \frac{\sum_w J_{w,2}\beta_x^w\sqrt{\beta_y^w}e^{i(2\Delta\phi_{w,x}-\Delta\phi_{w,y})}}{16[1-e^{2\pi i(2Q_x-Q_y)}]}$	(2,−1) skew sextupole
$f^{(1)}_{1101} = \frac{\sum_w J_{w,2}\beta_x^w\sqrt{\beta_y^w}e^{i(-\Delta\phi_{w,y})}}{8[1-e^{2\pi i(-Q_y)}]}$	(0,1) skew sextupole

these series are truncated. RDTs depend on the strengths of the corresponding magnets $\vec{K} = (\delta K_1, J_1, K_2, J_2, K_3, \ldots)$ where δK_1 is the quadrupole error field not included in the computation of the C-S parameters, J_1 is the skew quadrupole field, K_2 and J_2 are the normal and skew sextupole fields, K_3 refers to the octupole and so on. First-order RDTs $f^{(1)}$ result from Lie series truncated to the first term, are generated by the specific corresponding magnet, as in Table III, and scale linearly with their strengths. Schematically they may be represented by the following chart

$$\begin{aligned}
\text{focusing errors } f^{(1)} &\longleftarrow \delta K_1\\
\text{betatron coupling } f^{(1)} &\longleftarrow J_1\\
\text{normal sextupole } f^{(1)} &\longleftarrow K_2\\
\text{skew sextupole } f^{(1)} &\longleftarrow J_2\\
\text{normal octupole } f^{(1)} &\longleftarrow K_3.
\end{aligned} \tag{1}$$

When the Lie series are truncated to the second order, cross-products between the magnet strengths appear and the picture becomes more complicated for the second-order RDTs $f^{(2)}$

$$\begin{aligned}
\text{focusing errors } f^{(2)} &\longleftarrow J_1 \otimes J_1\\
\text{betatron coupling } f^{(2)} &\longleftarrow J_1 \otimes \delta K_1\\
\text{normal sextupole } f^{(2)} &\longleftarrow K_2 \otimes \delta K_1, J_1 \otimes J_2\\
\text{skew sextupole } f^{(2)} &\longleftarrow J_2 \otimes \delta K_1, J_1 \otimes K_2\\
\text{normal octupole } f^{(2)} &\longleftarrow K_3 \otimes \delta K_1, K_2 \otimes K_2 \ldots
\end{aligned} \tag{2}$$

The above scheme simplifies considerably under three reasonable assumptions. First, if the C-S parameters (β and ϕ) used in Table III are evaluated from the lattice model including focusing errors, $\delta K_1 \equiv 0$. Second, no strong skew sextupole is installed or powered in the machine and J_2 is generated by slightly tilted normal sextupoles, $K_2 \gg J_2$ and $J_1 \otimes J_2 \simeq 0$, betatron coupling being also weak. Third, coupling is assumed to be weak so that $J_1 \otimes J_1 \simeq 0$. The above RDTs then reduce to

$$\begin{aligned}
\text{focusing errors } & f^{(1)}=0, \quad f^{(2)}=0 \\
\text{betatron coupling } & f^{(1)} \leftarrow J_1, \quad f^{(2)}=0 \\
\text{normal sextupole } & f^{(1)} \leftarrow K_2, \quad f^{(2)}=0 \\
\text{skew sextupole } & f^{(1)} \leftarrow J_2, \quad f^{(2)} \leftarrow J_1 \otimes K_2 \\
\text{normal octupole } & f^{(1)} \leftarrow K_3, \quad f^{(2)} \leftarrow K_2 \otimes K_2
\end{aligned} \tag{3}$$

These considerations (detailed mathematical derivations may be found in Appendix A and Ref. [12]) indicate that the first-order analytic formulas for coupling and normal sextupole RDTs of Table III are valid also to the second order, provided that the used C-S parameters (β and ϕ) are evaluated from the lattice model including focusing errors. By doing so, first-order beta-beating RDTs are automatically zero.

Second-order terms are instead to be computed and included in the evaluation of skew sextupole RDTs, which are excited to the first order by J_2 (introduced by tilted sextupoles and/or displaced octupoles), and to the second order by the cross-product between coupling and normal sextupoles, $K_2 \otimes J_1$. In machines with strong focusing, such as light sources, strong normal sextupole (K_2), even if multiplied by low (i.e., well corrected) coupling (J_1), render the second-order contribution to the skew sextupole RDTs comparable to that of the first order, i.e., $K_2 \otimes J_1 \simeq J_2$. Similar considerations apply for octupolar RDTs.

Another complication appearing when second-order terms are to be taken into account is that RDTs $f = f^{(1)} + f^{(2)}$ are no longer observables from the harmonic analysis of turn-by-turn position data. The observable RDTs (ORDTs) g_{jklm} may be written as

$$g_{jklm} = f^{(1)}_{jklm} + f^{(2)}_{jklm} + \mathbf{L}(f^{(1)}_{pqrt} \otimes f^{(1)}_{uvwz}), \tag{4}$$

where $\mathbf{L}$ is a linear function and $jklm \neq pqrt \neq uwvz$. For this reason in Table I the ORDTs g_{jklm} replace the first-order $f^{(1)}_{jklm}$ in the four lines corresponding to skew sextupole harmonics. Formulas for the computation of the ORDTs from the lattice model are derived in Appendix A and may be easily implemented numerically. An example may help clarify the nature of $\mathbf{L}$ and reveal a counterintuitive feature: The skew sextupole ORDT g_{0030} reads

$$\begin{array}{ccccc}
g_{0030} = & f^{(1)}_{0030} & + f^{(2)}_{0030} & - \frac{i}{3}\left[f^{(1)}_{1010} f^{(1)}_{0120} - f^{(1)*}_{1001} f^{(1)}_{1020}\right], \\
& \uparrow & \uparrow & \uparrow \\
& J_2 & J_1 \otimes K_2 & J_1 \otimes K_2
\end{array} \tag{5}$$

$$f^{(2)}_{0030} = i \frac{\tilde{h}^{(2)}_{0030} + \hat{h}_{0030}}{1 - e^{2\pi i (3Q_y)}}, \tag{6}$$

where $\tilde{h}^{(2)}(s)_{0030}$ and $\hat{h}_{0030}$ are computed in Eqs. (A22) and (A24), respectively, whereas all other first order RDTs $f^{(1)}$ are defined in Table III. The counterintuitive feature exhibited by the additional term $\mathbf{L}(f^{(1)} \otimes f^{(1)})$ is that a skew sextupole resonance, the (0,3) in the case of g_{0030}, may be excited even in the absence of skew sextupole sources $f^{(1)}_{0030} = 0$ and far away from the resonant condition $1 - e^{2\pi i (3Q_y)} \simeq 1$ and $f^{(2)}_{0030} \simeq 0$, for example in the presence of large coupling and close to the difference resonance $|f^{(1)}_{1010}| \ll |f^{(1)}_{1001}| \sim 1$, since $|g_{0030}| \sim \frac{1}{3}|f^{(1)}_{1020}|$ and the normal sextupole RDT $f^{(1)}_{1020}$ may be arbitrarily large. The effect of betatron coupling and sextupole resonances has been known since more than two decades [22,23].

In summary, the CRDTs F are measurable from turn-by-turn position data (Table II). They may be also computed from the model (fourth column of Table I) via the first-order RDTs (Table III) or, if second-order contributions may not be neglected, via the ORDTs of Appendix A. The logical scheme to be followed in the nonlinear lattice modeling discussed in this paper is the following:

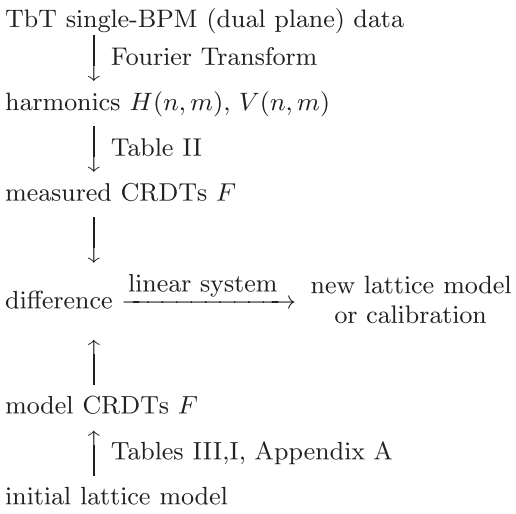

B. Experimental precautions

An important condition necessary to ensure the applicability of the single-BPM TbT data analysis is that monitors are dual-plane. In fact, in order to extract the CRDTs the knowledge of amplitude ($2I$) and phase (ψ_0) of both tune lines is mandatory, which in turn requires the possibility of measuring TbT data in both planes at the same BPM. Another requirement is that the beam does not experience decoherence, otherwise additional factors are to be included, as discussed in Ref. [5]. A further condition is that BPMs have no tilt or calibration error. Uncalibrated BPMs would provide TbT data in the form of $\tilde{x}(N)^{BPM} = \eta_x \tilde{x}(N)$, where $\eta_x \neq 1$. The amplitude of all spectral lines of Table I would then be multiplied by η and the formulas of Table II would no longer apply.

The amplitude of the tune lines, $|H(1,0)| = 1/2\sqrt{2I_x}$ and $|V(0,1)| = 1/2\sqrt{2I_y}$, shall be constant along the ring, as indicated by the first two lines of Table I. If this is not the

case, there are three possible causes to be evaluated and removed prior to any further analysis involving other spectral lines.

First, the linear lattice model used to evaluate the β functions at the BPMs is incorrect. The mismatch between model and real β functions would result in a modulation of the amplitude of the tune lines along the ring. By comparing and fitting the measured BPM phase advance, a reliable focusing model may be built and used to evaluate correctly the beta functions at the BPMs. As discussed in Sec. V, some octupolar CRDTs may perturb the phase of the tune lines, though this effect may be controlled by a careful choice of the initial excitation (i.e., kicker strength). It is worthwhile to recall that the fit of the BPM phase advance shall be accompanied by a fit of the measured dispersion function for a reliable model.

Second, if a modulation persists even after fitting the BPM phase advance (and dispersion), it shall be verified whether octupole and (second-order) sextupole terms may introduce a dependence on the longitudinal position. As discussed in Appendix B, this perturbation depends on the initial oscillation amplitude (or the action), i.e., on the kicker strength, and may be evaluated from preliminary single-particle tracking simulations. For the measurement procedure discussed here, it is hence necessary to limit the kicker strength so to keep the natural modulation of the tune line amplitude induced by sextupoles well below the desired experimental resolution. This contrasts with the desire of having a large signal-to-noise ratio between spectral noise and amplitude of the sextupolar lines, which would require a strong initial excitation. Eventually a trade off shall be found with the help of tracking simulations and measured data at different kicker strengths.

The third source of tune line amplitude modulation is represented by BPM calibration factors $\eta \neq 1$ and tilts. Assuming that the latter are negligible compared to other sources of errors, the only way to infer η and remove them before carrying out the spectral analysis is to impose constant tune line amplitude at all BPMs after having verified the previous two points. The Fourier transform redone after scaling the measured data by η may then be used for the analysis of the nonlinear model.

A last interesting figure to evaluate the quality of the TbT BPM data and of their harmonic analysis is represented by a cancellation condition that shall be satisfied by some measured CRDTs. According to the definitions of the normal sextupole terms of Table I it is straightforward to prove that

$$F_0 = 2\Re\{F_{NS2}\} - \Re\{F_{NS1}\} + \Re\{F_{NS0}\} \equiv 0 \quad (7)$$

anywhere in the ring: the closer F_0 is to zero, the more reliable is the harmonic analysis described here. Note that the measured F_0 along the ring depends only on: (i) the linear lattice model (β functions used to normalize the BPM TbT data); (ii) the BPM calibration factors, spatial and spectral resolution, and electronic noise; (iii) initial beam excitation, i.e., kicker strength. Luckily enough, it does not depend on the nonlinear lattice model, being valid for any sextupole setting.

C. From normal sextupole CRDTs to sextupole errors

Let us assume to have acquired TbT data from N_{BPM} BPMs. From the harmonic analysis of Table II it is possible to infer the four normal sextupole CRDTs F_{NS3}, F_{NS2}, F_{NS1}, and F_{NS0}, at all BPMs. Since these are all complex quantities, a $N_{\mathrm{BPM}} \cdot 4 \cdot 2$ vector $\vec{F}_{NS,\mathrm{meas}}$ may be defined containing the measured real and imaginary parts of the four CDRTs

$$\begin{aligned}\vec{F}_{NS,\mathrm{meas}} = (&\Re\{F_{NS3}\}_1, \ldots, \Re\{F_{NS3}\}_{N_{\mathrm{BPM}}}, \\ &\Im\{F_{NS3}\}_1, \ldots, \Im\{F_{NS3}\}_{N_{\mathrm{BPM}}}, \\ &\ldots, \\ &\Im\{F_{NS0}\}_1, \ldots, \Im\{F_{NS0}\}_{N_{\mathrm{BPM}}}). \end{aligned} \quad (8)$$

An equivalent vector may be defined from the model (C-S parameters including focusing errors, β and ϕ, and sextupole integrated gradients, K_2): The RDTs f_{3000}, f_{1200}, f_{1020}, f_{0120}, and f_{0111} may be evaluated from Table III, to be used for the evaluation of the model CRDTs through the fourth column of Table I. Being all passages from the integrated strengths to the CRDTs linear, the model vector may be defined as

$$\vec{F}_{NS,\mathrm{mod}} = \mathbf{M_{NS}}\vec{K}_2, \quad (9)$$

where $\vec{K}_2$ contains all N_{sext} known sources of sextupolar field along the ring, and $8 \cdot N_{\mathrm{BPM}} \times N_{\mathrm{sext}}$ matrix $\mathbf{M_{NS}}$ depends on the linear lattice only, through the β functions, the phase advances between BPMs and sextupoles and the tunes. The difference between measured and model CRDTs then reads

$$\vec{F}_{NS,\mathrm{meas}} - \vec{F}_{NS,\mathrm{mod}} = \mathbf{M_{NS}}\vec{\Delta K}_2, \quad (10)$$

where $\vec{\Delta K}_2$ contains the N_{sext} sextupole field errors to be inferred after pseudoinverting (via SVD, for instance) the above linear system. Note how the choice of defining the CRDTs vector with the real and imaginary parts ensures the linearity of the system, whereas the choice of decomposing these complex quantities in amplitude and phases, as in Ref. [9], would have introduced an unnecessary and avoidable nonlinearity in the problem, thus requiring a nonlinear minimization routine for the evaluation of $\vec{\Delta K}_2$.

The linear system of Eq. (10) may be also used for the calibration of an individual sextupole. The optics model in this case is necessary for the evaluation of the $(8 \cdot N_{\mathrm{BPM}}) \times 1$ *matrix* $\mathbf{M}$ only, whereas the left-hand side contains two CRDT vectors measured with two different sextupole strengths, i.e.,

$$\vec{F}_{NS,\mathrm{meas}}(K_2) - \vec{F}_{NS,\mathrm{meas}}(K_2 + \delta K_2) = \mathbf{M_{NS}}\delta K_2. \quad (11)$$

After pseudoinverting the above system, the inferred δK_2 may be compared with the expected value from the change of current in the sextupole and its calibration curve. The latter may be reconstructed and compared with the magnetic model (or measurement) by repeating the procedure at different δK_2. Again, the problem of calibrating a nonlinear magnetic element is reduced to a linear system when looking at the CRDTs.

D. From normal sextupole CRDTs to sextupole correction

The natural extension of Eq. (10) is a system for the evaluation of a sextupole corrector setting. If all sextupole magnets have independent power supplies and other sources of sextupolar fields (such as fringe fields in bending magnets) may be neglected, the pseudoinversion of Eq. (10) already provides the set of corrections $\overrightarrow{\delta K}_2$ to insert in the sextupoles. If this is not the case and only N_{cor} corrector sextupoles are available (which is the case at the ESRF storage rings, with 224 sextupoles grouped in 7 families and only 12 sextupole correctors available), the system then reads

$$\vec{F}_{NS,\mathrm{meas}} - \vec{F}_{NS,\mathrm{ref}} = \mathbf{M_{NS,cor}}\vec{K}_2^{\mathrm{cor}}, \quad (12)$$

where $\vec{K}_2^{\mathrm{cor}}$ contains the strengths of the N_{cor} sextupole correctors to be evaluated after pseudoinverting the above system, and the $8 \cdot N_{\mathrm{BPM}} \times N_{\mathrm{cor}}$ matrix $\mathbf{M_{NS,cor}}$ depends on the β functions and the phase advances between BPMs and the correctors. Note that $\vec{F}_{NS,\mathrm{ref}}$ (reference or desired vector) has been used in place of $\vec{F}_{NS,\mathrm{mod}}$ (model vector). The difference may be of importance for those machines (like the ESRF storage ring) where beta-beating is corrected up to some percents and special insertion optics break up significantly the machine natural periodicity. $\vec{F}_{NS,\mathrm{ref}}$ may refer hence to the ideal lattice without any insertion optics, whereas $\vec{F}_{NS,\mathrm{mod}}$ refers to the actual model including insertion optics (if any) and all known lattice errors. It is assumed here that the best CRDT correction shall be based on the ideal vector $\vec{F}_{NS,\mathrm{ref}}$, rather than on $\vec{F}_{NS,\mathrm{mod}}$. Once more, the problem of correcting nonlinear magnetic elements is reduced to a linear system, Eq. (12), to be pseudoinverted.

E. From skew sextupole CRDTs to sextupole tilts

The procedure described in the Sec. III D may be repeated, with some precautions, for the evaluation of sextupole tilts. From the harmonic analysis of the TbT BPM data and Table II it is possible to infer the four skew sextupole CRDTs F_{SS3}, F_{SS2}, F_{SS1}, and F_{SS0}, at all BPMs, and cast them in a $N_{\mathrm{BPM}} \cdot 4 \cdot 2$ vector $\vec{F}_{SS,\mathrm{meas}}$

$$\begin{aligned}\vec{F}_{SS,\mathrm{meas}} = (&\Re\{F_{SS3}\}_1, \ldots, \Re\{F_{SS3}\}_{N_{\mathrm{BPM}}},\\ &\Im\{F_{SS3}\}_1, \ldots, \Im\{F_{SS3}\}_{N_{\mathrm{BPM}}},\\ &\ldots,\\ &\Im\{F_{SS0}\}_1, \ldots, \Im\{F_{SS0}\}_{N_{\mathrm{BPM}}}).\end{aligned} \quad (13)$$

The evaluation of the corresponding vector from the model requires a preliminary step. As discussed in Sec. III A, contrary to normal sextupole terms, it is not possible to ignore the second-order contribution to the skew sextupole CRDTs due to cross terms between coupling and normal sextupole RDTs, see Eq. (3). In other words, ideal skew sextupoles CRDTs shall all be zero, but even with perfectly upright sextupoles they may be nonzero because any residual coupling in the machine *transfers* normal sextupole spectral harmonics in the other plane, hence generating skew sextupole harmonics and corresponding CRDTs. Not taking into account this natural contribution would corrupt the evaluation of sextupole tilts. For this reason new analytic formulas valid to second order have been derived. They are presented in Appendix A and shall be used for the evaluation of the skew sextupole ORDTs g_{jklm}, and hence of the CRDTs F_{SS}. Provided that betatron coupling is well modeled, the second-order contribution to the CRDTs F_{SS} may be then computed and any difference between the model vector $\vec{F}_{SS,\mathrm{mod}}$ and the measured one $\vec{F}_{SS,\mathrm{meas}}$ will depend on the sextupole tilts only, i.e.

$$\vec{F}_{SS,\mathrm{meas}} - \vec{F}_{SS,\mathrm{mod}} = \mathbf{M_{SS}}\vec{J}_2, \quad (14)$$

where the angles θ can be extracted from J_2 according to

$$\theta = -\frac{1}{3}\arcsin\left(\frac{J_2}{K_2}\right), \quad (15)$$

since the skew sextupole strength introduced by a tilted sextupole is $J_2 = -K_2 \sin(3\theta)$.

It is worthwhile to mention that measuring skew sextupolar CRDTs will be unavoidably more difficult than extracting normal sextupole CRDTs, the latter scaling with the (strong) sextupole gradients, while the former scale with the (small) sextupole tilts. Depending on the lattice configuration and coupling correction, $\vec{F}_{SS}$ may be one or two orders of magnitude lower than $\vec{F}_{NS}$.

In machines with skew sextupole correctors, the system of Eq. (12) may be modified as

$$\vec{F}_{SS,\mathrm{meas}} = -\mathbf{M_{SS,cor}}\vec{J}_2^{\mathrm{cor}}, \quad (16)$$

where the reference vector $\vec{F}_{SS,\mathrm{ref}}$ in this case is zero. In machines without skew sextupole correction, skew quadrupoles may be used to correct, along with coupling, skew sextupole CRDTs, via the second-order contributions $f^{(2)}_{jklm}$. This latter option, however, would require us to solve a more complex (but still linear in the skew quadrupole strengths) system not discussed here.

IV. EXPERIMENTAL RESULTS

A. Preparing measurements

The first natural preliminary step is to verify the synchronization of all 224 BPMs installed along the ESRF storage ring and to ensure that both kickers (horizontal and vertical) are synchronized so as to have the bunch train on their flattop: The measured invariants and CRDTs would be corrupted if the beam experiences the kicker pulse rise and/or fall.

The beam filling pattern and intensity are also optimized so as to have the best BPM resolution, this being of paramount importance in the analysis of spectral lines whose amplitudes are up to three orders of magnitude lower than the tune line. The chosen beam intensity will depend also on the range of excitation imparted to the beam. The beam is usually displaced horizontally to the beam from 1.3 to 5.5 mm. With a β function of 36.6 m this corresponds to an invariant between about 10^{-4} and 4×10^{-4} $\mathrm{m}^{1/2}$. Higher beam current would result in a different amplification range with lower digitization resolution, whereas stronger excitations risk to saturate the BPM signal.

As mentioned in Sec. III B the kicker strengths shall be a trade-off between spectral resolution (the stronger, the better) and second-order terms affecting the invariance of the tune line amplitude (the weaker, the better). Measurements are usually repeated at different kicker strengths. For the final analysis of sextupolar CRDTs only the data set of 50 repeated measurements with both invariants $\simeq 2.0 \times 10^{-4}$ $\mathrm{m}^{1/2}$ is used (corresponding to displacement of about 2.5 mm horizontally and 1.0 mm vertically, with β functions of 36.6 and 6.0 m, respectively). For the octupolar model, instead, data with stronger excitations are used. Note that hereafter, unless specified otherwise, the invariant is referred to as $1/2\sqrt{2I}$ so as to be equal to the tune line amplitude (see the first two rows in Table I).

As discussed in Sec. I, even though more than 2000 turns may be stored by the BPMs and the weak decoherence ensures about 1000 turns of exploitable data, it will be shown how the best results are obtained when only 256 turns are used for the analysis of sextupolar CRDTs (512 turns for the octupolar).

Throughout the paper, all RDTs and machine parameters (linear and nonlinear) from the *model* are evaluated by MADX-PTC [24].

B. Linear analysis of TbT BPM data

The starting linear optics model used to evaluate the expected CRDTs and the β functions at the BPMs (necessary for the construction of TbT signals to be analyzed $\tilde{x}(N) = x(N)/\sqrt{\beta_x}$ and $\tilde{y}(N) = y(N)/\sqrt{\beta_y}$) is based on the preliminary measurement and fit of the orbit response matrix (ORM) and dispersion [25]. As a figure of merit to assess the quality of the linear lattice model, the BPM phase advances are used: The smaller the deviation from the theoretical values, the better the model. At each pair of BPMs along the ring, the difference between measured and model phase advances may be evaluated and plotted. Its rms value over all BPMs may be also computed and used as a single figure of merit. In Fig. 3 an example is shown. If the ideal model without errors is used, large deviations are observed, with a rms of about 11 mrad. When the linear error model computed from the standard ORM measurement is used, the residual rms drops to about 7.5 mrad, with some remaining spikes in the vertical plane. On top of the ORM model, a response matrix on the BPM phase advance and dispersion was built and applied to the measured values to further reduce the deviation with the measured data. It is interesting to note how when going from the ideal model, to the one from the ORM, until the one matching the measured BPM phase advances, the rms variation along the ring of the tune line amplitude, i.e., of the invariant, is also reduced, as displayed in Table IV.

It is also worthwhile to notice how the residual rms error on the BPM phase advance has a minimum for the fifth data set of Table IV, with a kicker excitation so to generate an invariant of about 2×10^{-4} $\mathrm{m}^{1/2}$. Larger excitations seem to induce greater errors that could not be correlated to linear lattice elements. Octupolar terms affecting the tune lines may be the source of this larger discrepancy.

As far as the tune line amplitude variation along the ring is concerned, all data set with excitation lower than 2.6×10^{-4} $\mathrm{m}^{1/2}$ show a modulation of about 0.6% (with the TbT model, most right columns of Table IV and Fig. 4). Tracking simulations indicate that second-order sextupolar terms contribute a mere 0.1–0.2% of this modulation. Most of the discrepancy can be explained by small differences in the signal attenuation induced by BPM cables of different lengths, which introduces a modulation in the *sum* BPM signal similar to the one in the bottom plot of Fig. 5. Eventually, octupolar terms (unknown at this stage) may account for part of the observed modulation. For the sake of completion, effective BPM gains have been computed so as to cancel the tune line amplitude modulation corresponding

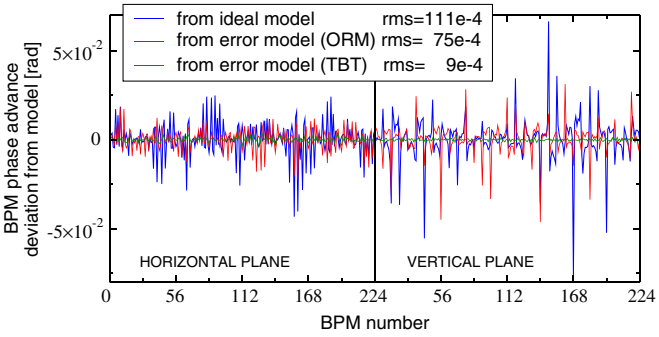

FIG. 3. Example of measured BPM phase advance deviation from the models: ideal (black), with errors inferred from ORM measurement (red) and with errors after fitting the measured BPM phase advance and dispersion (green). Data correspond to the fifth row of Table IV.

TABLE IV. Kicker strengths and corresponding invariants for the 8 sets of TbT BPM data (50 repeated acquisitions). The rms modulation of the tune line amplitude (i.e., of the invariant) and the rms deviation from the model BPM phase advance are measured with three different linear lattice models: ideal with no error, with errors inferred from precedent ORM measurement and fit, and from the harmonic analysis of TbT data. Horizontal and vertical data for the BPM phase advance are merged together when computing the rms deviation.

		Ideal lattice model		Model with errors (ORM)		Model with errors (TbT)	
(H,V) kicker strength (A, kV)	(H,V) mean invariant ($m^{1/2}$) $\times 10^{-4}$	(H,V) rms modulation ($m^{1/2}$) $\times 10^{-6}$	BPM phase advance rms error $\times 10^{-4}$ (rad)	(H,V) rms modulation ($m^{1/2}$) $\times 10^{-6}$	BPM phase advance rms error $\times 10^{-4}$ (rad)	(H,V) rms modulation ($m^{1/2}$) $\times 10^{-6}$	BPM phase advance rms error $\times 10^{-4}$ (rad)
(50, 1.0)	(0.52, 0.89)	(0.9, 1.6)	111	(0.7, 1.0)	75	(0.4, 0.4)	16
(100, 1.0)	(1.00, 0.90)	(1.7, 1.6)	110	(1.3, 1.0)	74	(0.7, 0.4)	13
(100, 1.5)	(1.00, 1.37)	(1.8, 2.4)	110	(1.3, 1.5)	74	(0.7, 0.7)	14
(200, 1.5)	(1.99, 1.42)	(3.5, 2.5)	111	(2.4, 1.6)	76	(1.4, 0.6)	11
(200, 2.1)	(2.01, 1.98)	(3.5, 3.5)	111	(2.4, 2.3)	75	(1.3, 0.9)	9
(250, 2.7)	(2.55, 2.58)	(4.5, 4.5)	111	(3.0, 3.3)	77	(1.7, 1.5)	12
(400, 2.5)	(4.11, 2.52)	(7.5, 4.8)	119	(4.8, 4.0)	91	(3.3, 2.2)	35
(400, 3.0)	(4.14, 2.98)	(7.5, 6.0)	118	(4.8, 5.0)	91	(3.5, 3.0)	36

to the fifth data set of Table IV, though they turned out to play a limited role in the nonlinear analysis.

Even though it is not used for the determination of linear lattice model, it is interesting to note how the CRDTs cancellation condition defined by F_0 of Eq. (7) is improved when the BPM phase advance is corrected. In general, the closer F_0 is to zero among all BPMs, the more accurate is the harmonic analysis. F_0 is evaluated with the CRDTs measured from the sextupolar spectral lines according to Table II. Its rms values (for the fifth data set of Table IV) goes from 4.4 $m^{-1/2}$ with the ideal linear model, to 4.3 $m^{-1/2}$ with the ORM error model, and eventually to 3.7 $m^{-1/2}$ with the model based on the BPM phase advance, even though large fluctuations among the 50 acquisitions are present, as shown in Fig. 6.

In conclusion, the linear analysis of the tune line (amplitude and phase) provided an effective linear model that improves considerably the quality of the harmonic analysis. The deviation between model and measured BPM phase advance is reduced by a factor greater than ten. The modulation of the tune line (i.e., of the invariant) is reduced from 2% to 0.6% or less. The cancellation term F_0 is reduced by about 20%. Effective BPM gains could be inferred from the tune line amplitude modulation.

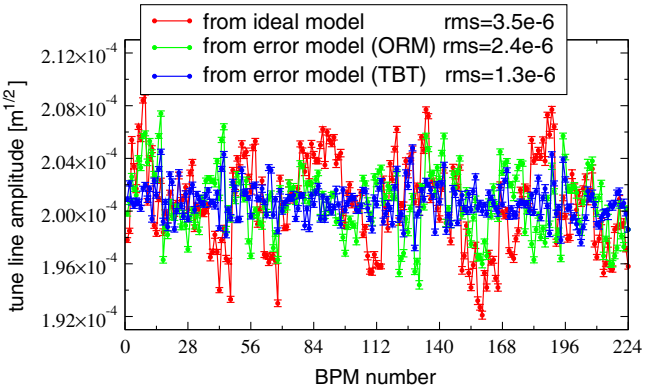

FIG. 4. Example of measured horizontal tune line amplitude (i.e., invariant) modulation along the ESRF ring when using different lattice models: ideal (black), with errors inferred from ORM measurement (red) and from TbT data plus dispersion (green). Rms values correspond to the fifth row of Table IV.

C. Nonlinear analysis of TbT BPM data

The effective linear lattice error model discussed in the previous section may now be used to evaluate the modulated

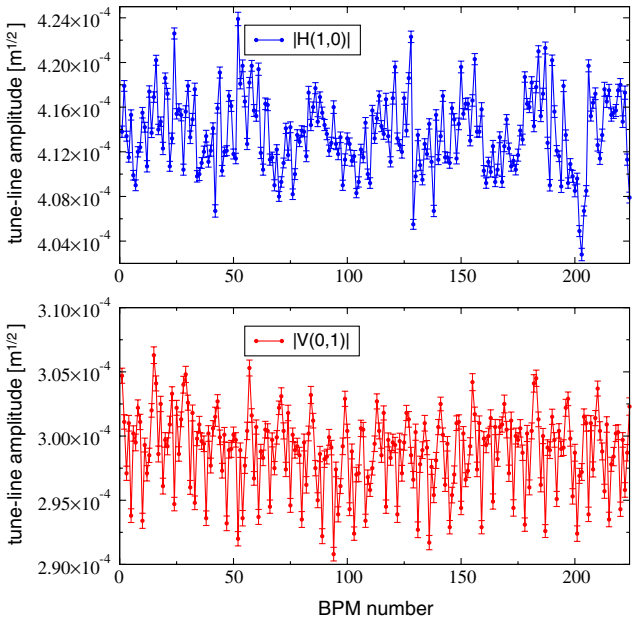

FIG. 5. Example of measured variation of the horizontal (top) and vertical (bottom) tune line amplitudes along the ESRF storage ring. Data correspond to the last row of Table IV (average over 50 acquisitions).

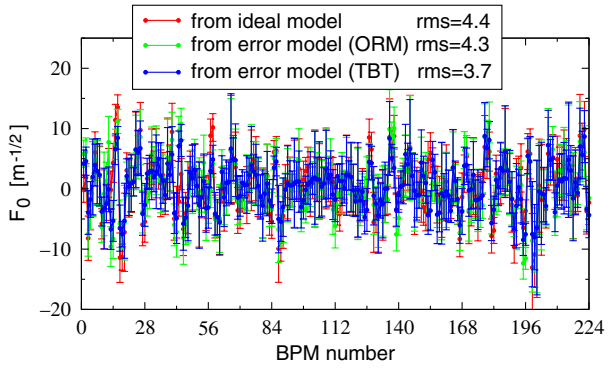

FIG. 6. Example of measured F_0 along the ESRF storage ring when different linear models (β functions at BPMs) are used: ideal lattice(black), with errors inferred from ORM measurement (red) and TbT data plus dispersion (green). Data correspond to the fifth row of Table IV (average over 50 acquisitions).

C-S parameters necessary to normalize the TbT data (β functions) and to evaluate the model CRDTs from Tables III and I. The measured CRDTs are instead inferred from the sextupolar lines $H(-2,0)$, $H(0,-2)$, and $V(\pm 1,-1)$ according to Table II. These lines are represented in blue in the example of measured spectra of Fig. 7. As for the linear analysis, a data set among those acquired at different kicker strengths is to be chosen, considering that a too weak excitation may affect the measurement because of the low signal-to-noise ratio, whereas a too strong excitation may introduce high-order terms not included in the present analysis. As discussed in Sec. III B, the nonlinear analysis presented here is valid as long as the CRDT residual F_0 of Eq. (7) is much lower than the average CRDT amplitudes. The rms values of F_0 (computed after averaging among the 224 BPMs and the 50 acquisitions) for each data set and for different linear lattice models are reported in Table V.

Because of the ESRF storage ring tune working point ($Q_x = 36.440$ and $Q_y = 13.390$) two sextupolar lines, $H(0,-2)$ and $V(-1,-1)$, necessary for the evaluation of as many CRDTs receive a contribution from higher-order octupolar terms, as shown in Fig. 7. A complete list of the octupolar spectral lines will be given in Sec. V. If not taken into account or avoided, this superposition will corrupt the CRDT measurement and the overall nonlinear model. Even though it is not possible to disentangle the individual contributions, the CRDT residual F_0 may be evaluated: the closer to zero, the less detrimental are the octupolarlike terms. Another way out may be found by slightly detuning the machine so as to ensure a sufficient separation between these lines: By setting for example $Q_x = 36.438$ and $Q_y = 13.385$ a separation of 0.022 in tune units would be assured. In the acquired data (at nominal tunes) the mean value of F_0 is always very close to zero (between -0.4 and 0.8 $\mathrm{m}^{-1/2}$, depending on the data set). The lowest rms F_0 (3.7 $\mathrm{m}^{-1/2}$) is obtained for an excitation corresponding to a mean invariant (in both planes) of 2.0×10^{-4} $\mathrm{m}^{1/2}$. The CRDTs measured from this data set are then used for the nonlinear lattice modeling.

As for the linear analysis, a figure of merit needs to be defined to quantify the goodness of the sextupole model. The difference between the measured CRDT vector and the one for model may be used to this end. The rms value of this vector, i.e., the residual $\mathcal{R}$, provides a figure of merit for the model,

$$\text{residual } \mathcal{R} = \sqrt{\langle |\vec{F}_{NS,\mathrm{meas}} - \vec{F}_{NS,\mathrm{mod}}|^2 \rangle} = \sqrt{\frac{1}{N}\sum_{i=1}^{N} (F_{NS,\mathrm{meas}}(i) - F_{NS,\mathrm{mod}}(i))^2}, \quad (17)$$

where $N = 8 \cdot N_{\mathrm{BPM}}$ [the 4 CRDTs are complex quantities, separated in real and imaginary parts, see Eq. (8)]. It is worthwhile to notice that $\mathcal{R}$ depends greatly on the lattice: Different machines and optics may result in different residuals for a similarly good sextupole model. In order to compare different storage rings or settings, the residual may be normalized by the mean CRDT amplitude.

A convenient way to display measured and model CRDTs is to separate their phase and amplitude. In the

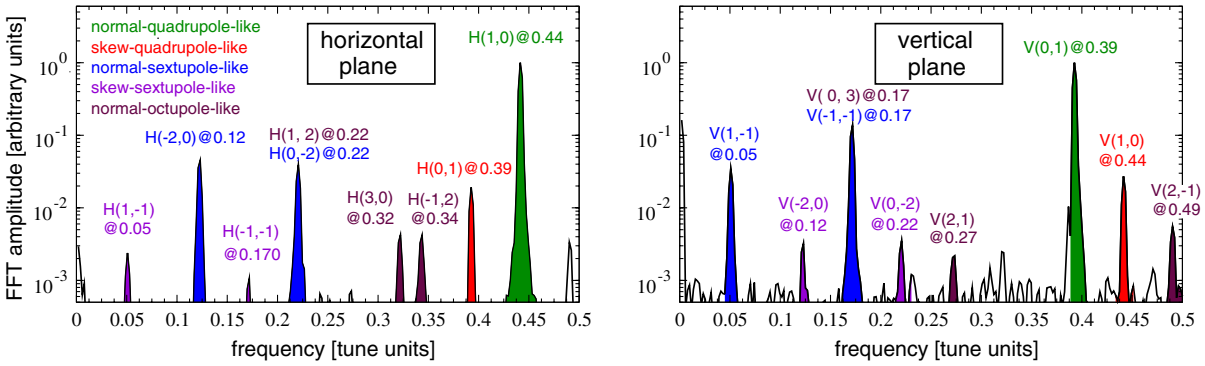

FIG. 7. Example of horizontal (left) and vertical (right) spectral lines inferred from the FFT of TbT BPM data measured after exciting transversely the beam with the strongest kicker strengths of Table V. A special sextupole setting was used to reduce detuning with amplitude and chromaticity and to enhance the normal sextupole spectral lines. Higher-order octupolarlike lines (in maroon) are also excited and measurable, though they may overlap the sextupolarlike, corrupting the CRDTs measurement and resulting in large F_0.

TABLE V. Measured rms variation along the ESRF storage ring of F_0 against different lattice models (i.e., β functions at BPMs) for all acquired data sets. The mean value is between −0.4 and 0.8 depending on the set (50 acquisition each, FFT over 256 turns).

		rms F_0 ($m^{-1/2}$)		
(H,V) kicker strength (A, kV)	(H,V) mean invariant $m^{1/2} \times 10^{-4}$	Ideal lattice model	Error model (ORM)	Error model (TbT)
(50, 1.0)	(0.52, 0.89)	8.4	8.8	8.5
(100, 1.0)	(1.00, 0.90)	5.6	5.9	5.4
(100, 1.5)	(1.00, 1.37)	4.8	5.0	4.4
(200, 1.5)	(1.99, 1.42)	4.4	4.4	3.9
(200, 2.1)	(2.01, 1.98)	4.4	4.3	3.7
(250, 2.7)	(2.55, 2.58)	5.1	4.9	4.3
(400, 2.5)	(4.11, 2.52)	7.8	7.5	7.5
(400, 3.0)	(4.14, 2.98)	7.9	7.6	7.6

left plot of Fig. 8 the measured CRDT phases are shown together with the corresponding expectation from the ideal model of the ESRF storage ring. The agreement is already remarkable, as are the small statistical error bars. When comparing the CRDT amplitude instead (right plot of Fig. 8), the 16-fold periodicity of the ideal curves is modulated in the measured CRDTs. The overall residual is $\mathcal{R} = 7.7\ m^{-1/2}$.

Interestingly, in an earlier analysis based on a sextupole calibration curve measured in 2001 the initial residual was about 10% higher ($\mathcal{R} = 8.4\ m^{-1/2}$) and the magnetic errors inferred from the measured CRTDs yielded suspiciously large errors in some sextupole families. This curve was indeed obtained after cycling a spare sextupole to 250 A. On the other hand, those installed in the ring (mechanically and magnetically identical to the spare one, with a few exceptions) are grouped in seven families (3 chromatic and 4 harmonic) subjected to different cyclings: close to 250 A for the chromatic sextupoles, between 120 and 150 A for the harmonics. These facts triggered a new campaign of magnetic measurements in 2012, reproducing in the laboratory the different cyclings. These new calibration curves are used since then for this analysis, resulting in the smaller initial residual of $\mathcal{R} = 7.7\ m^{-1/2}$ and in much lower errors in the harmonic sextupoles. This was the first evidence of the predicting power of this new technique.

The observed modulation of the CRDT amplitudes on top of the 16-fold periodicity is greatly reproduced after introducing in the model the linear lattice errors, as shown in the left plot of Fig. 9. The modulated β functions and phase advances seem to be an important source, the residual $\mathcal{R}$ dropping by more than 60% to $3.2\ m^{-1/2}$. It should be mentioned that the ESRF storage ring suffers from large β beating (about 2–3% rms) compared to more recent third generation light sources (well below 1%), because only 32 corrector quadrupoles are available for its correction (out of 256 magnets grouped in 6 families). The modulation of the CRDT amplitudes in other machines, then, shall depend greatly on their level of β beating. As far as the ESRF storage ring is concerned, this second-order effect of quadrupole errors on sextupole resonances generates in some regions CRDTs of about 50% (up to 100% for the vertical CRDT F_{NS0}) larger than in an ideal machine (see right plot of Fig. 8). This may have a considerable impact on the dynamic aperture of the ring (the larger the CRDTs, the greater the phase space distortion), independently on any possible sextupole error.

Before performing the SVD pseudoinversion of the linear system of Eq. (10) to infer sextupole errors, the measured CRDTs are compared to the model after introducing sextupolar fields in the 64 main bending magnets. Measurements performed on prototypes in the early 90s [26] indicated an integrated sextupole field of

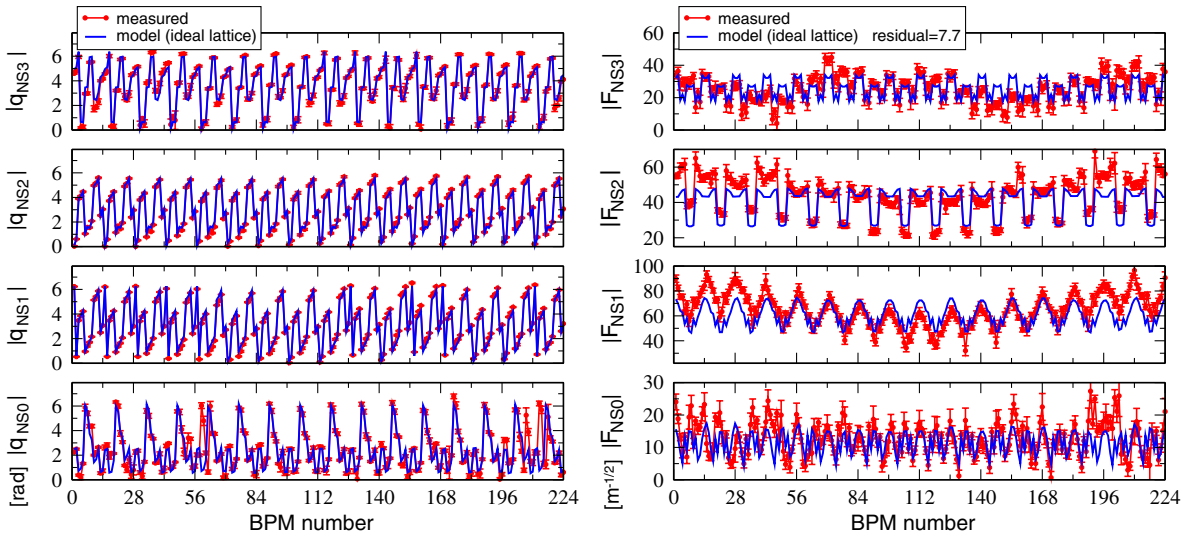

FIG. 8. Red: CRDT phases (left) and amplitudes (right) measured at the ESRF storage ring (with a special dedicated optics). Blue: the same quantities computed from the ideal perfect lattice. The residual for this model is $\mathcal{R} = 7.7\ m^{-1/2}$.

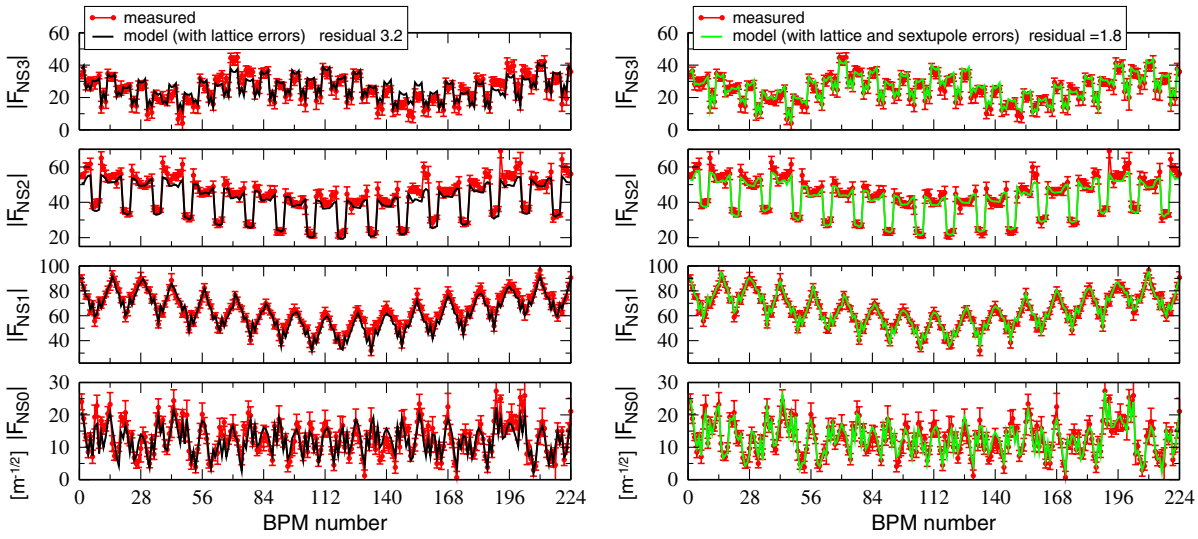

FIG. 9. Amplitudes of normal sextupole CRDTs (red curves) measured at the ESRF storage ring (with a special dedicated optics). Left: comparison with the model curves obtained from the lattice model comprising ideal sextupoles and focusing errors and coupling (residual $\mathcal{R} = 3.2$ m$^{-1/2}$). Right: comparison with the same linear model after introducing sextupole errors and sextupolar components in the main bending magnets ($\mathcal{R} = 1.8$ m$^{-1/2}$).

-1.8 ± 0.1 T/m. The plot of Fig. 10 shows how the residual $\mathcal{R}$ reaches a minimum with a field of -1.77 ± 0.09 T/m. The agreement is excellent, again confirming the reliability of this measurement.

Interestingly, when solving the system of Eq. (10) to evaluate the sextupole errors, the average error per family is reduced by about one order of magnitude after introducing the -1.77 T/m sextupole field in all 64 bending magnets, as reported in Table VI.

However, in both cases the sextupole family S4 seems to have a larger rms spread (0.8%) compared to other families (between 0.1% and 0.4%). The magnets exhibiting the largest deviations turned out to be the only four (recently installed) independent sextupoles, with a relative error of about -1.5%. These are shorter than the standard ones (20 cm instead of 40 cm) and have been displaced by 10 cm with respect to the nominal position so as to lengthen two straight sections. New positions and calibration curves have been included in the model (the integrated strength shall be the same of the standard S4 sextupoles). A more detailed analysis on these magnets is reported in Sec. IV E. When introducing the sextupole field in the bending magnets and fitting the 224 magnet errors by inverting the system of Eq. (10), the residual drops to $\mathcal{R} = 1.8$ m$^{-1/2}$: The corresponding CRDT amplitudes are displayed in the right plot of Fig. 9, while the errors (mean and rms of each family) are reported in the last column of Table VI: The great majority of the sextupole errors are well below the $\pm 1\%$ specification, as displayed in Fig. 11.

Of course, the inferred errors vary according to the parameters for the SVD pseudoinversion of Eq. (10). All the results shown in this section are derived by cutting the number of eigenvectors to 26 (out of 224): more vectors

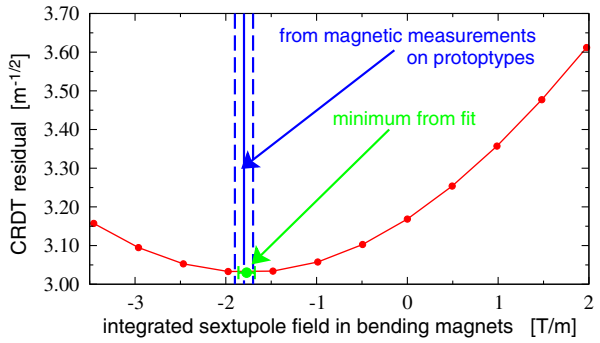

FIG. 10. Dependence of the residual $\mathcal{R}$ on the sextupolar component in bending magnets, where the blue line indicates the field measured on two prototypes. The residual is computed before introducing errors in the 224 sextupoles.

TABLE VI. Mean and rms sextupole field relative errors (per family) inferred from the CRDTs measurement. "Baseline model" includes bending magnets with no higher-order fields, whereas a sextupole component of -1.77 T/m is inserted in the model of the last column. This improves the overall residual $\mathcal{R}$ (see Fig. 10) and lowers the average errors in the 224 sextupoles by about one order of magnitude.

Relative error [%] (average $\pm$ rms) per family		
Family	with baseline model	with -1.77 T/m in bendings
S4	-0.12 ± 0.79	-0.02 ± 0.80
S6	0.20 ± 0.43	-0.02 ± 0.43
S13	-0.14 ± 0.34	0.02 ± 0.34
S19	0.04 ± 0.11	$\sim 0.0 \pm 0.11$
S20	-0.07 ± 0.11	0.01 ± 0.11
S22	0.24 ± 0.41	-0.03 ± 0.41
S24	-0.09 ± 0.41	0.01 ± 0.42

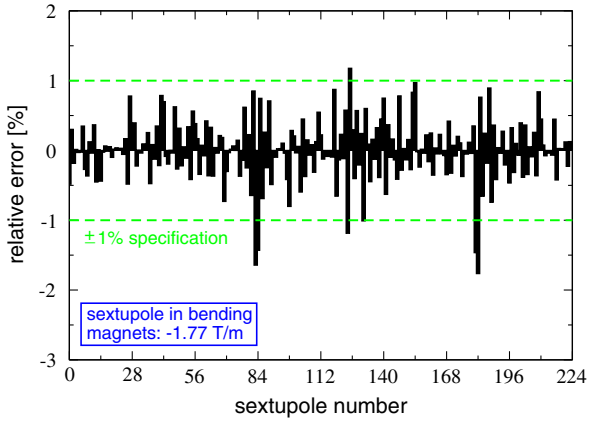

FIG. 11. Errors in the 224 sextupoles as computed from the (SVD) pseudoinversion of the system in Eq. (10). Quality specifications for those magnets are at ±1%. The SVD is performed with 26 (out of 224) eigenvalues and sextupoles are assumed to be perfectly positioned longitudinally. The residual with this set is $\mathcal{R} = 1.8\ \mathrm{m}^{-1/2}$. For each family, mean and rms errors are reported in the last column of Table VI.

induce a limited reduction of less than $0.1\ \mathrm{m}^{-1/2}$ in the final residual $\mathcal{R}$ at the expense of large sextupole errors, well beyond 1%.

The sextupole field errors of Fig. 11 are computed assuming that all 224 sextupoles are placed at their nominal longitudinal position along the ring. Any displacement along s, e.g., the circumference, would change the CRDTs through the β functions and phases ϕ (see Table III) because of the dependence of the latter on s. Part of the field errors attributed to the magnets by the CRDTs may actually be a combination of magnetic imperfection and longitudinal displacement. Periodic metrological surveys and adjustments are carried out at the ESRF storage ring twice per year. However, they ensure a state-of-the-art alignment on the transverse plane only. A longitudinal alignment was carried out in the early 1990s during the installation only, with specifications in the mm range. To understand the contribution of longitudinal displacements δs on the CRDTs and, hence, on the equivalent field errors in the sextupole, the response matrix of Eq. (10) was extended, namely

$$\vec{F}_{NS,\mathrm{meas}} - \vec{F}_{NS,\mathrm{mod}} = \mathbf{M_{NS}} \begin{pmatrix} w_K \cdot \overrightarrow{\delta K}_2 \\ w_s \cdot \overrightarrow{\delta s} \end{pmatrix}, \qquad (18)$$

where $\overrightarrow{\delta s}$ contains the $N_{\mathrm{sext}} = 224$ sextupole longitudinal displacements, whereas w_K and $w_s = 1 - w_K$ are introduced to weigh out the two contributions. $\mathbf{M_{NS}}$ is now a $8 \cdot N_{\mathrm{BPM}} \times 2 \cdot N_{\mathrm{sext}}$ response matrix. It has been observed that by allowing rms longitudinal displacement up to about 3 mm the magnetic errors drop by about 15%.

In Fig. 7 four spectral lines excited by skew sextupolar terms, $H(\pm 1, -1)$, $V(-2, 0)$, and $V(0, -2)$ are visible, hence measurable. Since no physical skew sextupole is installed in the machine, they are generated only by tilts of the main normal sextupoles (or their residual skew components) and by the cross product between residual coupling and normal sextupoles. The former is a first-order contribution, i.e., it can be well described by the RDTs f_{jklm} of Table III, whereas the latter is a second-order term that can be correctly described only by the second-order RDTs g_{jklm} of Table I, to be evaluated from the model as described in Table XIV of Appendix A. From these four spectral lines, skew sextupole CRDTs F_{SS} can be measured after applying the corresponding formulas of Table II. However, because of the low coupling and small sextupole rotations, the lines are about one order of magnitude lower than those excited by normal sextupoles (see Fig. 7). Hence, the signal-to-noise ratio becomes an issue and the measurement of the skew sextupole CRDTs is less reliable, as can be seen from the top left plot of Fig. 12 where the error bars (evaluated from the statistics over 50 acquisitions) are of the same order of magnitude of the baseline skew sextupole CRDTs. In order to enhance the signal-to-noise ratio of the four lines, another series of measurements have been taken after introducing large coupling, by powering a well-calibrated skew quadrupole corrector. By doing so, the second-order contribution to $\vec{F}_{SS,\mathrm{mod}}$ of Eq. (14) from g_{jklm} becomes dominant, though it can be evaluated from the model with great accuracy. The four skew sextupole spectral lines are now enhanced well above the noise level and the CRDT measurement becomes more reliable, with smaller error bars (in relative terms), as shown in the top right plot of Fig. 12. As done for the sextupole field error, the system of Eq. (14) may be pseudoinverted via SVD and an effective model of sextupole tilts may be inferred from Eq. (15). In the bottom left plot of Fig. 12 a model obtained with 35 out of 224 eigenvalues is displayed, with the corresponding CRDTs shown in the bottom right plot of the same figure.

The resulting rms sextupole rotation is of about 1.3 mrad, with some magnets exceeding ±3 mrad. Again, results vary according to the number of eigenvalues. However, metrological surveys ensure rms girder rotations well below 0.1 mrad and it is hard to believe that magnets installed onto them may account for more than 1 mrad. An alternative explanation for such large skew sextupole components has been proposed and is currently being investigated. During magnetic measurements of new quadrupole magnets a large skew quadrupole component was measured each time the two halves of the yoke were not properly aligned (see left picture of Fig. 13): For that specific magnet, as a rule of thumb, a horizontal displacement between the two yokes of 100 μm would generated a skew quadrupole field, corresponding to about 1 mrad equivalent rotation. This sensitivity is suspected to be of importance for sextupoles too, these being actually separated in three yokes (right picture of Fig. 13). Numerical simulations and magnetic measurements are planned to validate this conjecture. If confirmed, hence, the large skew sextupole components observed in

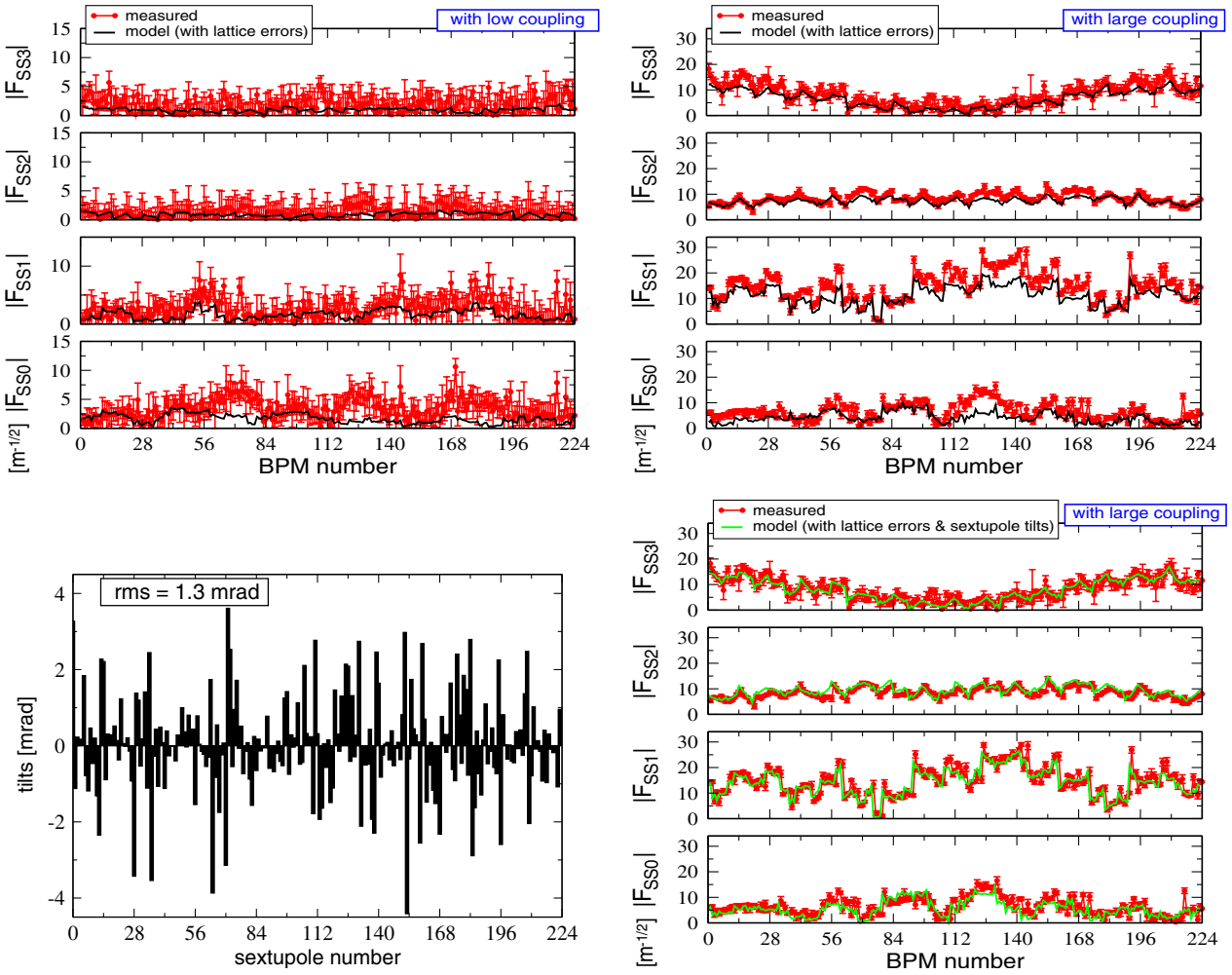

FIG. 12. Top: amplitude of skew sextupole CRDTs measured at the ESRF storage ring (red) and from the model with no sextupole rotation (black), with nominal low betatron coupling (left) and with larger coupling excited by a well-calibrated skew quadrupole (right). Bottom left: tilts the 224 sextupoles as computed from the (SVD) pseudoinversion of the system of Eq. (14) and from Eq. (15). The SVD is performed with 35 (out of 224) eigenvalues. Bottom right: model (green) and measured (red) CRDTs after introducing these tilts.

the ESRF storage ring may be induced by the limited precision in the assembly of the three sextupole yokes, rather than by the physical magnet rotation as a whole. Another source of skew sextupole components in the normal sextupoles is being investigated: As shown in the bottom picture of Fig. 13, the cooling circuit is such to generate a temperature gradient among the six poles and, in turn, mechanical and magnetic asymmetries. These are believed to induce additional multipole components, among which skew sextupoles.

D. Correction of sextupolar CRDTs

After building up a realistic sextupolar error model, the natural further step would be to use the measured CRDTs ($\vec{F}_{NS,\mathrm{meas}}$) and the desired one ($\vec{F}_{NS,\mathrm{ref}}$, from the ideal lattice model with no error), insert them in the linear system of Eq. (12), and pseudoinvert it to evaluate the strengths of the available sextupole correctors. The result of such an exercise is shown in Fig. 14, where the difference vector $\vec{F}_{NS,\mathrm{meas}}$-$\vec{F}_{NS,\mathrm{ref}}$ is plotted before and after the correction, together with the corresponding strengths of the 19 available sextupole correctors.

Even if elegant and efficient (the residual is almost halved with just 19 correctors out of 224 sources of errors), this approach is rather inconvenient. The main reason is that, while focusing errors and coupling may be evaluated and corrected routinely from ORM measurements, TbT BPM measurements are less obvious and difficult to perform with the same regularity.

A rapid look at the evolution of the residual $\mathcal{R}$ as a function of the lattice models may provide a handy, though not perfect, solution. Table VII summarizes this dependence. Because of the relatively large persistent β-beating in the ESRF storage ring, the main contribution to the measured CRDTs (~50%) originates from focusing errors, whereas only 25% seems to stem from sextupole errors and a further 25% is not accounted for (possibly because of

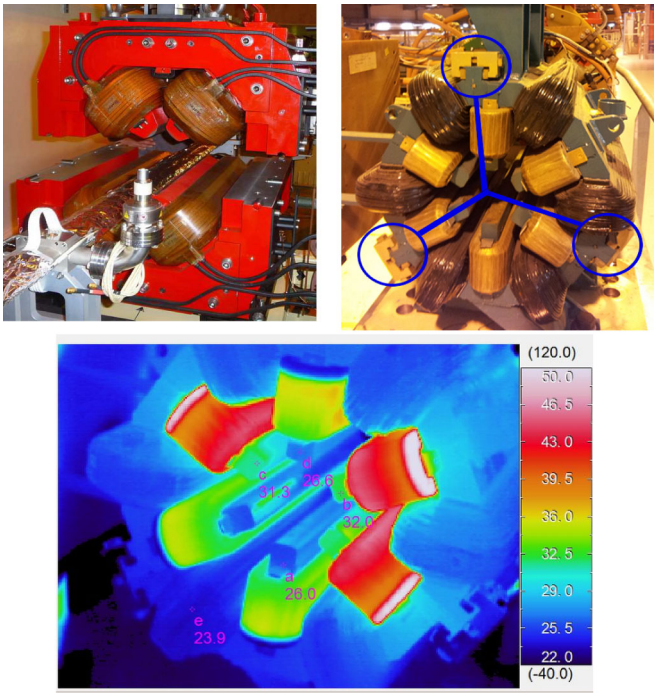

FIG. 13. Top: Mechanical assemblies of the ESRF magnets: Quadrupoles are separated in two halves (left), whereas three yokes are screwed together to create sextupoles (right) with survey monuments being placed on one arc only. Bottom: The infrared image of a sextupole in operation shows a difference of temperature among the six poles up to 5°C.

higher-order terms affecting the sextupolar spectral lines, as shown in Fig. 7). This means that a detailed linear lattice model would describe the true CRDTs with an accuracy sufficient for their rough correction, even ignoring sextupole errors. This corresponds to use and correct the black (model) curves in the left plot of Fig. 9 instead of the (measured) red curves: Even if not perfect, the model CRDTs may already be used for an effective and rapid correction. This may be a peculiarity of machines like the one at the ESRF. For more recent accelerators with independent magnets, and hence with much lower residual focusing errors, this may not be the case.

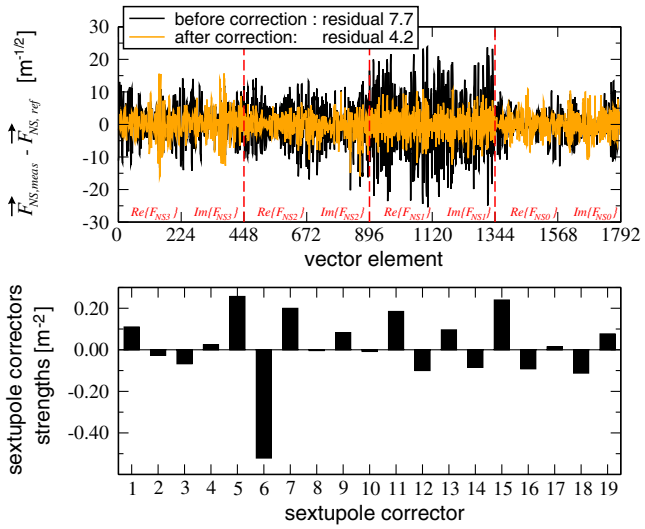

FIG. 14. Example of normal sextupole CRDT correction. Top: Difference between the measured and the reference CRDT vectors before (black) and after (orange) correction. Bottom: Integrated strengths of the corresponding 19 available sextupole correctors.

To verify this conjecture, a test during machine-dedicated time was carried out. The software application for the measurement of the ORM and correction of focusing and coupling errors was modified to compute the normal sextupole CRDTs from the lattice model (i.e., from Tables III and I) including focusing errors and coupling, generating the $\vec{F}_{NS,\mathrm{meas}}$ vector. The ideal C-S parameters were instead used to compute the ideal CRDTs, $\vec{F}_{NS,\mathrm{ref}}$. In both cases sextupoles with no error were used. The system of Eq. (12) was then pseudoinverted to infer the strengths of the sextupole correctors. This procedure was applied to a standard multibunch optics optimized for a train of 868 bunches (7/8 of the storage ring circumference) filled with 200 mA (i.e. 0.23 mA per bunch). To enhance the Touschek effect which is believed to be presently the main limitation for the lifetime, another filling pattern with 192 bunches, each of about 1 mA, was stored. With all sextupole correctors turned off and a vertical emittance $\epsilon_y = 7.1$ pm ($\epsilon_x = 4$ nm), a lifetime of 16.2 hours was measured. After applying the standard manual optimization of the four sextupolar resonance stop bands, the lifetime reached 24.2 hours. When the strengths computed automatically from Eq. (12) were used, the measured lifetime was 22.4 hours. This proved the effectiveness of the method, which can be used for a first correction from scratch before trimming the correctors by hand with the standard ESRF procedure. Nevertheless, it turned out to be not yet optimal. Another test was carried out to a different optics with higher chromaticity (to stabilize higher charges per bunch) and clearly showed a poorer performance of the CRDT correction compared to the standard procedure. The reason for this dependence on the implemented optics has not been yet understood.

TABLE VII. Residual $\mathcal{R}$ of Eq. (18) between the measured normal sextupole CRDTs and different lattice models.

Model characteristics	Residual $\mathcal{R}$ [m$^{-1/2}$]
ideal lattice + 2001 sextupole calibration	8.4
ideal lattice + 2012 sextupole calibration	7.7
lattice with focusing errors + 2012 sextupole calibration	3.2
lattice with focusing errors + 2012 sextupole calibration + sextupole errors	1.8

E. Beam-based calibration of independent sextupoles via CRDTs

As discussed in the last paragraph of Sec. III D, the measurement of CRDTs F_{NS} may be repeated for different gradients of individual sextupoles or correctors to obtain a calibration curve, (integrated) strength vs. current. The ESRF storage ring comprises of 224 sextupoles mostly grouped in seven families, each sharing a common power supply. Six new short magnets recently installed to lengthen three straight sections are fed independently, and two standard sextupoles have been stripped out and paired on a single power supply. The correction of sextupolar resonances is carried out by twelve correctors (trim coils) hosted in as many magnets of the families S24 (eight) and S20 (four). Even though magnetically identical, because of the different working points, the (stronger) chromatic S20 are close to saturation, whereas the (weaker) harmonic S24 are still in the linear regime. This results in trim coils with different calibration curves, i.e., the slopes C_f of the linear curve $K_2 = C_f \cdot I$, where I denotes the imparted current.

By measuring the CRDTs it is then possible to validate the calibration of both the trim coils and the six independent short sextupoles S4. The first check is necessary for the effectiveness of the automatic resonance correction discussed in the previous section, whereas the latter is to confirm the hypothesis raised in Sec. IV C of having short sextupoles weaker than expected.

For two trim coils in cell 8 (S20C8 and S24C8) the measurement has been carried out with several points and the calibration coefficient is obtained from a linear fit of the curve $K_2 = C_f \cdot I$. As shown in the upper plots of Fig. 15 the agreement with the model is nearly perfect for the corrector S20C8, and compatible within 10% for S24C8. The same measurement was then repeated for the other ten correctors. Results are reported in the bottom chart of Fig. 15. Because of the limited available machine time, the linear fit for the remaining ten correctors was carried out with two points only, at ± 1 A. Between each measurement, magnets were not cycled and the persistence of some remaining magnetic fields could not be excluded. If these arguments may explain the poorer agreement between standard model and measured coefficients for these ten correctors, they cannot justify the large discrepancy observed for two trim coils, in S24C23 and S24C29, respectively. As far as the corrector in cell 23 is concerned, the explanation is rather simple: As of 2013 the standard 40 cm long main magnet has been replaced by a new short type. As a result, the calibration for its corrector is almost halved (C_f from 0.443 to 0.239 $\mathrm{A}^{-1}\,\mathrm{m}^2$), consistent with the measured value. In the case of the trim coils of S24C29, thanks to this measurement, a mismatch was indeed found between the power supplies (recent 2-A types) and one of the two driver cards (still set for an old 5-A type). This incongruity resulted in a corrector about 30% weaker than normal (C_f from 0.443 to 0.310 $\mathrm{A}^{-1}\,\mathrm{m}^2$), again consistent with measurements. Following these findings, the software driving the trim coil S24C23 has been updated, and the driver card of S24C29 was reprogrammed.

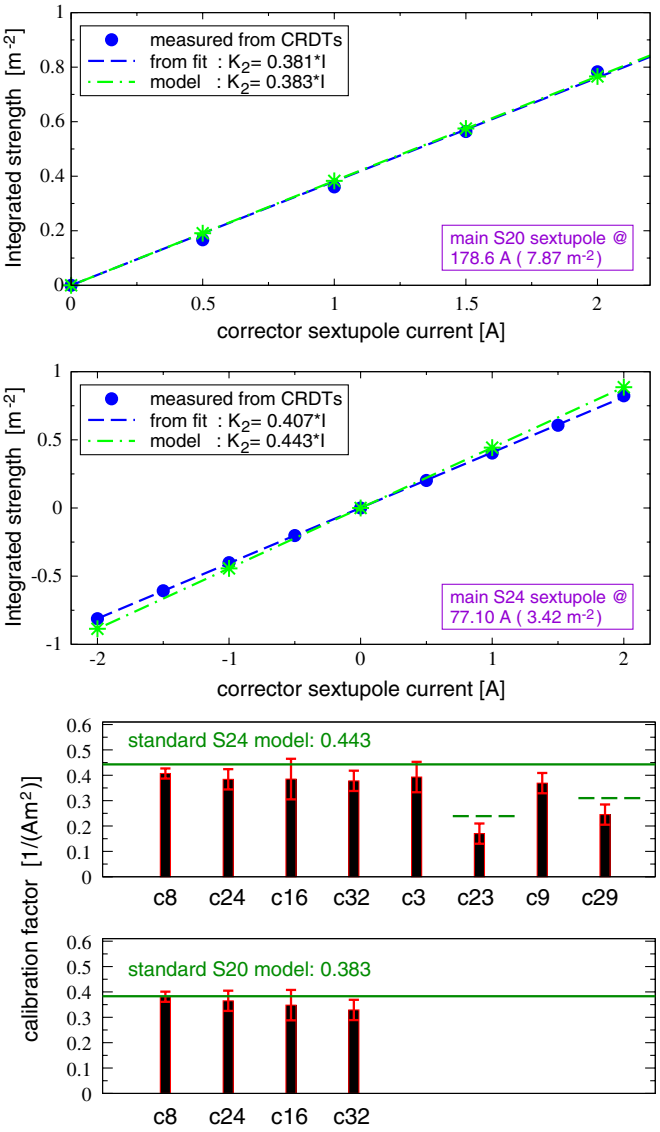

FIG. 15. Beam-based calibration of sextupole correctors (trim coils) from measurements of CRDTs and Eq. (11). For two correctors in cell 8 of the ESRF storage ring the curves have been measured in detail with several points: S20C8 is hosted in a chromatic sextupole (top plot) close to saturation, hence with a coefficient lower than in the correctors installed in the harmonic sextupoles, such as S24C8 (center plot), which are still in the linear regime. The measured coefficients (i.e., the slopes of the above plots) for all twelve trim coils are reported in the bottom chart.

Results from the same measurement carried out for one of the six new (short and independent) sextupole in cell 15, S4C15, are reported in Fig. 16. This beam-based calibration ($C_f = 0.0238 \pm 0.002$ $\mathrm{A}^{-1}\,\mathrm{m}^2$) is compatible with magnetic measurement ($C_f = 0.0241$).

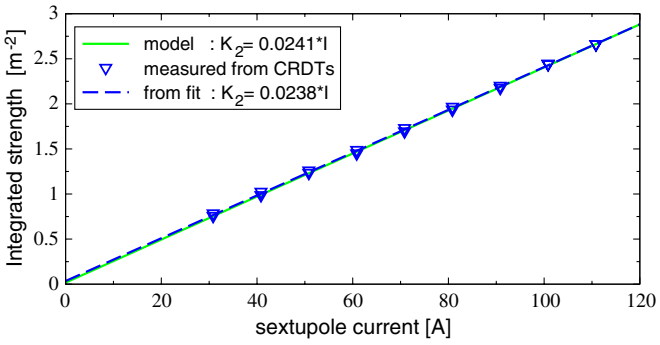

FIG. 16. Beam-based calibration of the short independent sextupole S4C15 from measurements of CRDTs and Eq. (11).

V. GOING BEYOND: OCTUPOLAR SPECTRAL LINES, CRDTS, AND MODELING

Figure 7 reveals the existence of four spectral lines well above noise level (and hence measurable) excited by octupolar CRDTs, namely $H(3,0)$, $H(-1,2)$, $V(2,1)$, and $V(2,-1)$. As shown in the same figure and described in Table VIII, two additional lines are excited by these terms, $H(1,2)$ and $V(0,3)$. However, the latter are indistinguishable from the sextupolar lines $H(0,-2)$ and $V(-1,-1)$, respectively, because of the tune working point. Hence the corresponding CRDTs F_{NO4} and F_{NO5} of Table VIII are not observable in our case. The best setting for the ESRF storage ring turned out to be the last of Table IV, with the horizontal kicker fired at 400 A and the

TABLE VIII. List of lines in the spectra of $\tilde{x}(N)$ and $\tilde{y}(N)$ excited by normal octupole CRDTs $F = |F|e^{iq_F}$ and excited resonances. For each line (defined as in Table I), expressions for its amplitude and phase are given. The tune lines $H(1,0)$ and $V(0,1)$ are also affected by octupolar terms that are however not observable. Quadrupole errors are to be included in the model when computing the Courant-Snyder (C-S) parameters used to evaluate $\tilde{x}(N)$, $\tilde{y}(N)$ and the CRDTs g_{jklm}, which are defined in Table XV.

Spectral line	Amplitude	Phase ϕ	Combined RDT	Resonances	Magnetic term
$V(0,3)$	$(2I_y)^{3/2}\lvert F_{NO5}\rvert$	$q_{F_{NO5}} + \frac{\pi}{2} + 3\psi_{y0}$	$F_{NO5} = 4g^*_{0040} - g_{0013}$	(0,4),(0,2)	y^4
$H(1,2)$	$(2I_x)^{1/2}(2I_y)\lvert F_{NO4}\rvert$	$q_{F_{NO4}} + \frac{\pi}{2} + \psi_{x0} + 2\psi_{y0}$	$F_{NO4} = 2g^*_{2020,H} - g_{1102}$	(2,2),(0,2)	x^2y^2
$H(3,0)$	$(2I_x)^{3/2}\lvert F_{NO3}\rvert$	$q_{F_{NO3}} + \frac{\pi}{2} + 3\psi_{x0}$	$F_{NO3} = 4g^*_{4000} - g_{1300}$	(4,0),(2,0)	x^4
$H(-1,2)$	$(2I_x)^{1/2}(2I_y)\lvert F_{NO2}\rvert$	$q_{F_{NO2}} - \frac{\pi}{2} - \psi_{x0} + 2\psi_{y0}$	$F_{NO2} = 2g_{2002} - g^*_{1120}$	$(2,-2),(0,2)$	x^2y^2
$V(2,-1)$	$(2I_x)(2I_y)^{1/2}\lvert F_{NO1}\rvert$	$q_{F_{NO1}} - \frac{\pi}{2} + 2\psi_{x0} - \psi_{y0}$	$F_{NO1} = 2g_{0220} - g^*_{2011}$	$(2,-2),(2,0)$	x^2y^2
$V(2,1)$	$(2I_x)(2I_y)^{1/2}\lvert F_{NO0}\rvert$	$q_{F_{NO0}} + \frac{\pi}{2} + 2\psi_{x0} + \psi_{y0}$	$F_{NO0} = 2g^*_{2020,V} - g_{0211}$	(2,2),(2,0)	x^2y^2

TABLE IX. Formulas to evaluate octupolar CRDTs from the secondary lines in the spectra of $\tilde{x}(N)$ and $\tilde{y}(N)$ assuming properly calibrated BPMs, turn-by-turn oscillations without decoherence and quadrupole errors included in the C-S parameters.

Combined RDT	Amplitude	Phase q_F
$F_{NO5} = \lvert F_{NO5}\rvert e^{iq_{F_{NO5}}}$	$\lvert F_{NO5}\rvert = \lvert V(0,3)\rvert/[8\lvert V(0,1)\rvert^3]$	$q_{F_{NO5}} = \phi_{V(0,3)} - 3\phi_{V(0,1)} - \frac{\pi}{2}$
$F_{NO4} = \lvert F_{NO4}\rvert e^{iq_{F_{NO4}}}$	$\lvert F_{NO4}\rvert = \lvert H(1,2)\rvert/[8\lvert H(1,0)\rvert\lvert V(0,1)\rvert^2]$	$q_{F_{NO4}} = \phi_{H(1,2)} - \phi_{H(1,0)} - 2\phi_{V(0,1)} - \frac{\pi}{2}$
$F_{NO3} = \lvert F_{NO3}\rvert e^{iq_{F_{NO3}}}$	$\lvert F_{NO3}\rvert = \lvert H(3,0)\rvert/[8\lvert H(1,0)\rvert^3]$	$q_{F_{NO3}} = \phi_{H(3,0)} - 3\phi_{H(1,0)} - \frac{\pi}{2}$
$F_{NO2} = \lvert F_{NO2}\rvert e^{iq_{F_{NO2}}}$	$\lvert F_{NO2}\rvert = \lvert H(-1,2)\rvert/[8\lvert H(1,0)\rvert\lvert V(0,1)\rvert^2]$	$q_{F_{NO2}} = \phi_{H(-1,2)} + \phi_{H(1,0)} - 2\phi_{V(0,1)} + \frac{\pi}{2}$
$F_{NO1} = \lvert F_{NO1}\rvert e^{iq_{F_{NO1}}}$	$\lvert F_{NO1}\rvert = \lvert V(2,-1)\rvert/[8\lvert H(1,0)\rvert^2\lvert V(0,1)\rvert]$	$q_{F_{NO1}} = \phi_{V(2,-1)} - 2\phi_{H(1,0)} + \phi_{V(0,1)} + \frac{\pi}{2}$
$F_{NO0} = \lvert F_{NO0}\rvert e^{iq_{F_{NO0}}}$	$\lvert F_{NO0}\rvert = \lvert V(2,1)\rvert/[8\lvert H(1,0)\rvert^2\lvert V(0,1)\rvert]$	$q_{F_{NO0}} = \phi_{V(2,1)} - 2\phi_{H(1,0)} - \phi_{V(0,1)} - \frac{\pi}{2}$

TABLE X. Detuning coefficients and second-order chromaticity for the special lattice optics studied throughout this paper. Measured values are listed in the first column, whereas the corresponding numbers for the lattice model (all comprising the errors inferred in the previous sections) are reported in the second column. The model is presented in three flavors: thin (Tn) and thick (Tk) sextupoles, and with additional fringe fields in all magnets (Tk-FF). Octupolar fields are introduced in the 256 main normal quadrupoles to reproduce the measured coefficients (first) and the octupolar CRTDs (then), yielding to the values in the last column.

		Model without octupoles			Model with octupoles
Parameter	Measured	Tk-FF	Tk	Tn	Tk-FF
ν_{xx}' [m^{-1}]	2430 ± 30	−1396	−2515	4185	2364
ν_{xy}' [m^{-1}]	-470 ± 15	1289	−115	4962	−521
ν_{yy}' [m^{-1}]	4750 ± 50	3485	2518	8206	4846
$Q_{x''}$ [ ]	-683 ± 24	−649	−657	−522	−660
$Q_{y''}$ [ ]	-96 ± 17	−67	−74	−30	−82

vertical at 3.0 kV. The formulas of Table IX to infer the octupolar CRTDs from the spectral lines have been corrected in the analysis by using the tune line amplitudes averaged among all 224 BPMs, i.e., $|H(1,0)| \rightarrow \langle|H(1,0)|\rangle$ and $|V(0,1)| \rightarrow \langle|V(0,1)|\rangle$ in order to reduce the impact of octupolar terms on the tune line (see discussion in the last part of Appendix B).

Even though no physical octupole is installed in the ESRF storage ring, the nonlinear model including sextupoles (with errors and tilts) alone does not suffice to reproduce global nonlinear parameters such as amplitude dependent detuning $\nu' = \partial Q/\partial(2I)$, as reported in Table X and Fig. 17. The agreement between this model and measurements is however already good as far as the second-order chromatic terms $Q'' = \partial^2 Q/\partial\delta^2$ are concerned. No significant difference has been observed in the RDTs when representing sextupoles either as thin or thick elements and when including fringe fields. This is not the case for the global nonlinear parameters and in Table X values for the three different models are reported. All plots in this section refer to the thick model and including fringe fields.

To the first order, sextupoles do not drive any detuning with amplitude, which is a second-order effect (i.e., induced by cross-product between sextupole terms). Octupolar CRDTs too are excited by second-order sextupolar terms even in the absence of physical octupoles. This can be seen when comparing the four measured octupolar CRDTs with those evaluated from the lattice model (including all errors), as shown in the left plot of Fig. 18. Even though the global behavior is rather well reproduced by the model, a clear ingredient looks to be missing. Model CRDTs are evaluated by using the same procedure developed for the skew sextupole terms and described in Appendix A.

The first natural source of octupolar fields in a storage ring is represented by normal quadrupoles, because of the shape of their poles, fringe fields, and their geometry in two halves (any variation of the vertical distance between the two yokes generates octupolar fields). The linear lattice of the ESRF storage ring is based on eight quadrupoles per cell (256 magnets in total), with two pairs of identical magnets in the achromat fed by common power supplies, hence leaving six degrees of freedom. The first step in building the octupolar lattice model was to introduce six octupolar fields in the corresponding quadrupole families to best reproduce the five nonlinear parameters (three detuning coefficients and two second-order chromatic terms). The 256 octupole fields have been then adjusted independently so as to best reproduce the measured CRDTs of Fig. 18. As for the skew sextupole analysis, even though model and measured CRDTs are excited mainly by second-order contributions stemming from sextupoles, their difference will depend linearly on the octupolar field, and the same SVD pseudoinversion carried out in the previous sections may be generalized to octupoles. The results of such a fit are shown in the right plot of Fig. 18 as far as the

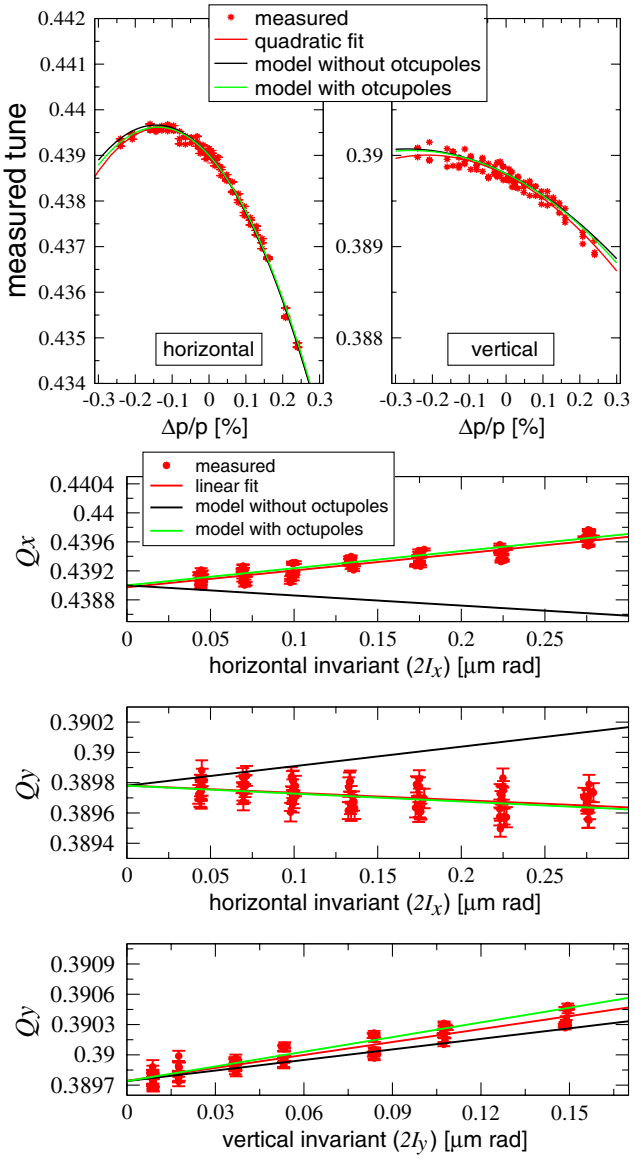

FIG. 17. Nonlinear chromaticity (top two graphs) and linear amplitude dependent detuning (bottom three plots). The measured curves (red) are compared to the ones computed from lattice model including all errors up to the sextupolar components (black), and after including octupolar components in the main quadrupoles (green). The corresponding coefficients are listed in the Tk-FF columns (thick sextupoles and fringe fields in all magnets) of Table X.

CRDTs are concerned, whereas the values of the global nonlinear parameters are reported in the last column of Table X and in Fig. 17.

The octupole integrated gradients K_3 (MADX definition) resulting from this analysis have been grouped for each quadrupole family and compared with the expectations from early magnetic measurements. Results are shown in Table XI. It is worthwhile to stress two caveats concerning such a comparison. First, measurements of high-order multipole components are available for six

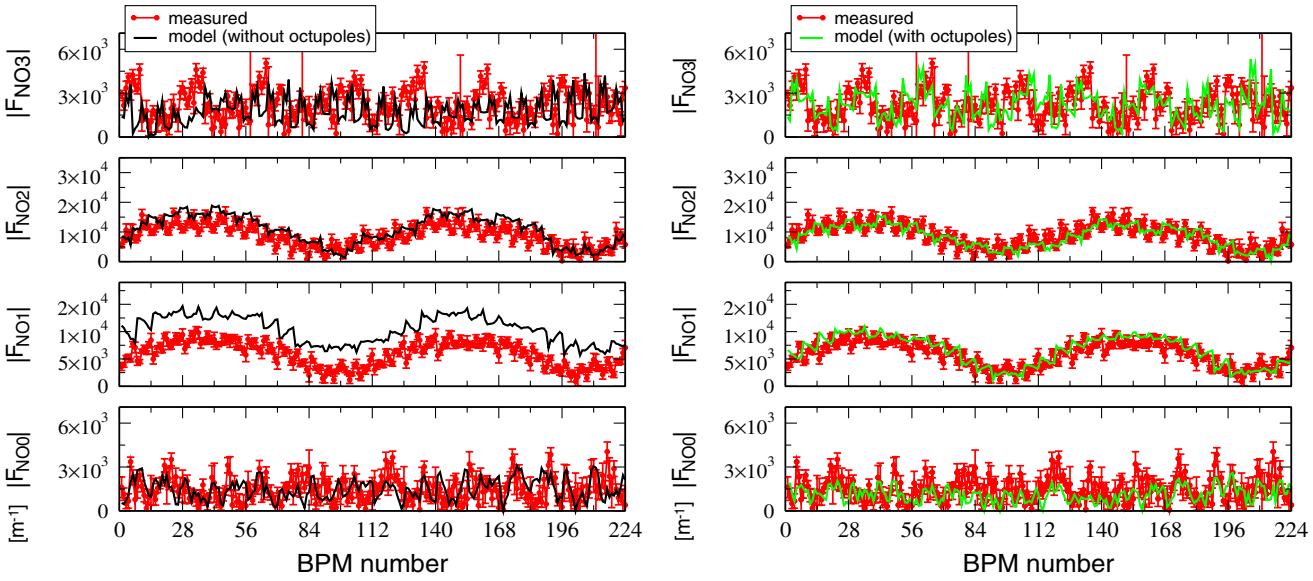

FIG. 18. Amplitudes of normal octupole CRDTs (red curves) measured at the ESRF storage ring (with a special dedicated optics). Left: comparison with the model curves obtained from a lattice with no octupolar source (CRDTs are excited by sextupoles to the second order only). Right: comparison with the same model after introducing octupole components in quadrupoles so as to fit the nonlinear parameters of Table X and the measured octupolar CRDTs.

quadrupoles only, out of 256, all taken at a fixed current of 222 A, whereas the six families operate within 217 and 492 A (near saturation). Second, the quadrupole mechanical assembly discussed in Sec. IV D and shown in Fig. 13 is such that there is an octupolar component dependent on the vertical separation between the two halves. Magnetic measurements carried out by the manufacturer [27] on the first batch of magnets showed a linear dependence and that for a vertical separation of 100 μm the values in the left column of Table XI would increase by 50%. The octupole polarity inferred for QD4 and QF5 families is inverse with respect to the magnetic measurements. Being these two families placed in the achromat next to the strong chromatic sextupoles, a contribution coming from the latter is suspected.

It shall be mentioned that measurements of octupolar CRDTs may be partially affected by BPM nonlinearities, these scaling with x^3 (y^3) to the first order [11] and the largest BPM data used for this analysis reaching about 6 mm. On the other hand, the software driving the ESRF BPMs computes the beam position using a nonlinear calibration curve, based on finite-element simulations of the BPM block, that accounts already for such nonlinearities.

TABLE XI. Mean and rms normal octupole component K_3 per quadrupole family. The first column refers to magnetic measurements (mag. meas.), while the second contains the values inferred from fitting the five nonlinear parameters of Table X and the measured octupolar CRDTs F_{NO} of Fig. 18.

Quadrupole family	K_3 [m^{-3}] from mag. meas.	K_3 [m^{-3}] from TbT analysis (average $\pm$ rms)
QF2	2.1 ± 0.8	4.4 ± 1.6
QD3	-1.8 ± 0.7	-6.9 ± 0.7
QD4	-1.4 ± 0.5	2.5 ± 0.8
QF5	2.2 ± 0.8	-2.2 ± 1.4
QD6	-3.4 ± 1.8	-0.4 ± 2.4
QF7	3.6 ± 1.3	4.0 ± 3.3

V. CONCLUSION

This paper has shown how the harmonic analysis of turn-by-turn data from beam position monitors may be exploited for the reconstruction and correction of machine nonlinearities up to octupolar terms. An important peculiarity of this approach is that the systems to be solved are always linear, even though they refer to nonlinear magnets. This represents a considerable step forward compared to preceding works on the same subject. Handy formulas have been derived and tested with real data for the quantitative evaluation of realistic magnetic model, for the calibration of individual nonlinear magnets and for the correction of the resonance driving terms. The analysis of the latter could predict the sextupolar field component measured in bending magnets, as well some inconsistencies with the calibration curves of sextupole magnets. Correcting sextupolar resonance driving terms in the ESRF storage ring with a low-chromaticity optics (for low-intensity multibunch modes) resulted in increased lifetime, though the gain was minimal when applied to optics with larger chromaticity (for high-intensity few-bunch filling patterns).

ACKNOWLEDGMENTS

We are grateful to the ESRF Operation Group for its support in preparing and carrying out measurements, to

F. Epaud for adjusting the BPM device server to our needs, to M. Dubrulle for setting up the kickers, to J. F. Bouteille for fruitful discussions and the infrared images of the sextupole magnets, and to F. Taoutaou for helping with the magnetic measurements. We are also indebted with R. Tomás for proofreading the original manuscript and making valuable suggestions.

APPENDIX A: NONRESONANT NORMAL FORMS AND RDTS UP TO THE 2ND ORDER

For a reliable analysis of the ESRF nonlinear lattice model, the normal form and RDT description of Refs. [4–7] needs to be extended to the second order. The theoretical background has been already developed in previous works, among which is the fundamental Ref. [28]. The first part of this appendix does not provide any further development to that work: Results of main interest in the context of this article are reported for the sake of consistency and nomenclature only. Mathematical proofs of the new results may be found in Ref. [12].

The turn-by-turn evolution of the complex C-S coordinates, $h_{q,\pm} = \tilde{q} \pm i\tilde{p}_q = \sqrt{2J_q}e^{\mp i(\phi_q+\phi_{q,0})}$, reads

$$\vec{h}_{s+C} = \tilde{\mathcal{M}}(s)\vec{h}_s, \quad \tilde{\mathcal{M}}(s) = e^{:\tilde{H}:}R, \quad e^{:\tilde{H}:} = \prod_{w=1}^{W} e^{:\tilde{H}_w:}, \tag{A1}$$

where $\vec{h} = (h_{x,+}, h_{x,-}, h_{y,+}, h_{y,-})$, C is the ring circumference, s is a generic position, and R denotes the phase-space rotation, whose frequencies are the betatron tunes. W is the total number of multipoles and the Hamiltonian term of the generic nonlinear magnet w reads

$$\tilde{H}_w(s) = \sum_{n\geq 2}\sum_{jklm}^{n=j+k+l+m} h_{w,jklm}e^{i[(j-k)\Delta\phi^{(s)}_{w,x}+(l-m)\Delta\phi^{(s)}_{w,y}]} \times h^j_{w,x,+}h^k_{w,x,-}h^l_{w,y,+}h^m_{w,y,-}, \tag{A2}$$

where $h_{w,q,\pm}$ is the coordinate at the generic magnet w, while $\Delta\phi^{(s)}_{w,q}$ is the phase advance between the latter and the observation point s. n denotes the magnet order: $n = 2, 3, 4$ for quadrupoles, sextupoles, and octupoles, respectively. The coefficients within the sums read

$$h_{w,jklm} = -\frac{[K_{w,n-1}\Omega(l+m) + iJ_{w,n-1}\Omega(l+m+1)]}{j!\quad k!\quad l!\quad m!\quad 2^{j+k+l+m}} \times i^{l+m}(\beta_{w,x})^{\frac{j+k}{2}}(\beta_{w,y})^{\frac{l+m}{2}},$$
$$\Omega(i) = 1 \quad \text{if } i \text{ is even}, \qquad \Omega(i) = 0 \text{ if } i \text{ is odd}. \tag{A3}$$

$\Omega(i)$ is introduced to select either the normal or the skew multipoles. $K_{w,n-1}$ and $J_{w,n-1}$ are the (MADX) integrated magnet strengths of the multipole expansion

$$-\Re\left[\sum_{n\geq 2}(K_{w,n-1} + iJ_{w,n-1})\frac{(x_w + iy_w)^n}{n!}\right]. \tag{A4}$$

If nonlinear terms are of relevance, at sufficiently large amplitudes the phase space is deformed from ellipses to more complex curves. In the case of normal sextupoles, the horizontal phase space (x, p_x) assumes a typical triangular shape, as a result of additional harmonics excited by these magnets (see Table I). The C-S transformation, being linear, will just remove the dependence on the linear parameters, rotating the triangle in an upright position and smoothing out its distortion. However, the invariant circle may not be retrieved, since the linear transformation may not *include* nonlinearities. The phase-space trajectory being still closed and regular, it must exist a transformation capable to retrieve a circle. Such transformation indeed exists and is a polynomial function F

$$F = \sum_{n\geq 2}\sum_{jklm}^{n=j+k+l+m} f_{jklm}\zeta^j_{x,+}\zeta^k_{x,-}\zeta^l_{y,+}\zeta^m_{y,-}, \tag{A5}$$

where n denotes the multipole order, f_{jklm} are the RDTs and $\zeta_{q,\pm} = \sqrt{2I_q}e^{\mp i(\psi_q+\psi_{q,0})}$ are the new complex normal form coordinates, which are the nonlinear generalization of the complex C-S complex variable of $h_{q,\pm}$. $(2I)$ is the nonlinear invariant, whereas ψ denotes the phase in normal form. The equation establishing the change of coordinates in normal form may be written in terms of Lie operators

$$e^{:\mathsf{H}:}R = e^{:-F:}e^{:\tilde{H}:}Re^{:F:} \tag{A6}$$

R is the same rotation of Eq. (A1), $\tilde{H} = \tilde{H}(J_x, J_y, \phi_x, \phi_y)$ is the phase-dependent Hamiltonian of Eq. (A1) (J and ϕ are the linear invariant and betatron phase), whereas $\mathsf{H}(I_x, I_y)$ is the phase-independent Hamiltonian in normal forms, with I the nonlinear invariant. Any dependence on the angles would indeed be related to the existence of fixed points different from the origin, around which stable orbits may exist, hence creating discontinuous phase space trajectories, as the ones of Ref. [29]: In this (resonant) case, no regular transformation may convert all separated trajectories in continuous circles.

Following the same procedure of Ref. [28], all operators may be decomposed in first- and second-order terms:

$$F = F^{(1)} + F^{(2)}, \tag{A7}$$

$$\mathsf{H} = \mathsf{H}^{(1)} + \mathsf{H}^{(2)}, \tag{A8}$$

$$\tilde{H} = \tilde{H}^{(1)} + \tilde{H}^{(2)} = \sum_{w=1}^{W}\tilde{H}_w + \frac{1}{2}\sum_{w=1}^{W}\sum_{u=1}^{w-1}[\tilde{H}_u, \tilde{H}_w]. \tag{A9}$$

Equation (A9) results from Eq. (A1): The composition of Lie operators indeed obeys to the Campbell-Backer-Hausdorff (CBH) theorem

$$e^{:A:}e^{:B:}e^{:C:} = e^{:A+B+C+\frac{1}{2}\{+[A,C]+[B,C]\}:} + O(3^{\mathrm{rd}}),$$

where [,] denotes the Poisson bracket, the first term (A + B + C) is the first-order truncation while the rest is the second-order contribution. Higher-order terms are here included in the reminder $O(3^{\mathrm{rd}})$. Being these operators polynomial functions, Eq. (A6) apply to all coefficients h_{jklm} (for $\tilde{H}$), f_{jklm} (for F), h_{jjll} (for H). The rotation R then will also act to each term $(\zeta_{x,+}^{j}\zeta_{x,-}^{k}\zeta_{y,+}^{l}\zeta_{y,-}^{m})$, i.e.

$$R = e^{2\pi i[(j-k)Q_x+(l-m)Q_y)]}, \quad \forall\ j,k,l,m. \tag{A10}$$

1. First-order RDTs

The normal form transformation up to the first order reads

$$\tilde{H}^{(1)\ddagger} = (I-R)F^{(1)} \Rightarrow F^{(1)} = \frac{\tilde{H}^{(1)\ddagger}}{I-R}, \tag{A11}$$

where $\tilde{H}^{(1)\ddagger}$ represents the phase dependent part of the C-S Hamiltonian. Recalling that both F and $\tilde{H}^{(1)}$ are polynomial functions [see Eqs. (A5) and (A2)], and the definition of R given in Eq. (A10), the above relation must hold for any index set j,k,l,m, i.e.,

$$f_{jklm}^{(1)}(s) = \frac{\sum_w h_{w,jklm}e^{i[(j-k)\Delta\phi_{w,x}^{(s)}+(l-m)\Delta\phi_{w,y}^{(s)}]}}{1-e^{2\pi i[(j-k)Q_x+(l-m)Q_y]}}. \tag{A12}$$

Note that the dependence on the phase of $\tilde{H}^{(1)\ddagger}$ implies that first-order RDTs f_{jjll} do not exist, as they would be phase-independent. The presence of the phase advances between the location where f_{jklm} is either evaluated or measured (s) and the one of the magnet w implies that RDTs vary along the ring. Formulas in Table III are derived from Eqs. (A12) and (A3).

To complete the normal form approach, explicit formulas for the change of coordinates are missing. They are readily derived from

$$\vec{h}(s,N) = e^{:F^{(s)}:}\vec{\zeta}(s,N). \tag{A13}$$

The Lie operator may be expanded as a Taylor series

$$e^{:F:}\vec{\zeta} = \vec{\zeta} + [F,\vec{\zeta}] + \frac{1}{2}[F,[F,\vec{\zeta}]] + O(3^{\mathrm{rd}}), \tag{A14}$$

where the reminder contains higher-order Poisson brackets. After truncating to the first Poisson bracket the complex C-S coordinates read

$$h_{x,-}(s,N) = \sqrt{2I_x}e^{i(2\pi Q_x N+\psi_{s,x,0})} - 2i\sum_{jklm} j f_{jklm}^{(s)}(2I_x)^{\frac{j+k-1}{2}}(2I_y)^{\frac{l+m}{2}}e^{i[(1-j+k)(2\pi Q_x N+\psi_{s,x,0})+(m-l)(2\pi Q_y N+\psi_{s,y,0})]}, \tag{A15}$$

$$h_{y,-}(s,N) = \sqrt{2I_y}e^{i(2\pi Q_y N+\psi_{s,y,0})} - 2i\sum_{jklm} l f_{jklm}^{(s)}(2I_x)^{\frac{j+k}{2}}(2I_y)^{\frac{l+m-1}{2}}e^{i[(k-j)(2\pi Q_x N+\psi_{s,x,0})+(1-l+m)(2\pi Q_y N+\psi_{s,y,0})]}, \tag{A16}$$

from which Table IV of Ref. [7] is derived.

In conclusion, up to the first order, Eq. (A12) is the formula to evaluate the RDTs from the lattice parameters, while Eqs. (A15) and (A16) may be used to compute (or measure) them from the FFT of turn-by-turn position data, either simulated via tracking or measured by BPMs. Both approaches provide the same equivalent RDTs. In the following part it will be shown how this equivalence is no longer true when second-order terms are to be taken into account.

2. Second-order RDTs

The second-order term of the normal form transformation reads

$$F^{(2)} = \left(\tilde{H}^{(2)\ddagger} + \frac{1}{2}\left[\mathsf{H}^{(1)}, \frac{I+R}{I-R}\tilde{H}^{(1)\ddagger}\right] + \frac{1}{2}\left[\tilde{H}^{(1)\ddagger}, \frac{\tilde{H}^{(1)\ddagger}}{I-R}\right]^{\ddagger}\right)/(I-R). \tag{A17}$$

If first-order detuning terms (generated by focusing errors and octupolar terms) are negligible some simplifications may be applied: The first-order Hamiltonian in the complex C-S coordinates will always be phase-dependent, i.e., $\tilde{H}^{(1)\ddagger} \equiv \tilde{H}^{(1)}$, $\mathsf{H}^{(1)} = 0$ and $[\tilde{H}^{(1)\ddagger}, \frac{\tilde{H}^{(1)\ddagger}}{I-R}]^{\ddagger} = [\tilde{H}^{(1)}, \frac{\tilde{H}^{(1)}}{I-R}]$, simplifying the above equation to

$$F^{(2)} = \left(\tilde{H}^{(2)\ddagger} + \frac{1}{2}\left[\tilde{H}^{(1)}, \frac{\tilde{H}^{(1)}}{I-R}\right]\right)/(I-R). \tag{A18}$$

The assumption of having no detuning term in the first-order Hamiltonian ($\mathsf{H}^{(1)} = 0$) shall not be confused with the unnecessary assumption of having zero linear detuning, that may come from sextupolar terms in the second-order Hamiltonian ($\mathsf{H}^{(2)} \neq 0$). The second-order C-S Hamiltonian $\tilde{H}^{(2)}$ reads

$$\tilde{H}^{(2)}(s) = i\sum_{w=1}^{W}\sum_{u=1}^{w-1}\Bigg\{\sum_{jklm}\sum_{pqrt} h_{w,jklm}h_{u,pqrt}e^{i[(p-q)\Delta\phi_{u,x}^{(s)}+(r-t)\Delta\phi_{u,y}^{(s)}+(j-k)\Delta\phi_{w,x}^{(s)}+(l-m)\Delta\phi_{w,y}^{(s)}]} \times [(jq-kp)h_{x,+}^{j+p-1}h_{x,-}^{k+q-1}h_{y,+}^{l+r}h_{y,-}^{m+t} + (lt-mr)h_{x,+}^{j+p}h_{x,-}^{k+q}h_{y,+}^{l+r-1}h_{y,-}^{m+t-1}]\Bigg\}. \tag{A19}$$

In general only those sets of index $jklm$ and $pqrt$ in Eq. (A19) satisfying the following relations shall be evaluated and summed up

$$\tilde{H}_{abcd}^{(2)}(s) = i\{\tilde{h}_{abcd}^{(2)}(s)\}h_{x,+}^{a}h_{x,-}^{b}h_{y,+}^{c}h_{y,-}^{d} \Rightarrow \begin{cases} j+p-1=a \\ k+q-1=b \\ l+r=c \\ m+t=d \end{cases} \text{ or } \begin{cases} j+p=a \\ k+q=b \\ l+r-1=c \\ m+t-1=d \end{cases}. \tag{A20}$$

An example may be of help in understanding this procedure. Let us evaluate the skew sextupolelike Hamiltonian term $\tilde{H}_{0030}^{(2)}$. According to Eqs. (A19) and (A20), the possible combinations of indexes $jklm$ and $pqrt$ generating a term proportional to $h_{y,+}^{3}$ must satisfy the following conditions

$$\tilde{H}_{0030}^{(2)}(s) = i\{\tilde{h}_{0030}^{(2)}(s)\}h_{y,+}^{3} \Rightarrow \begin{cases} j+p-1=0 \\ k+q-1=0 \\ l+r=3 \\ m+t=0 \end{cases} \text{ or } \begin{cases} j+p=0 \\ k+q=0 \\ l+r-1=3 \\ m+t-1=0 \end{cases}, \tag{A21}$$

resulting in

$$\begin{aligned}\tilde{H}_{0030}^{(2)}(s) &= i\{\tilde{h}_{0030}^{(2)}(s)\}h_{y,+}^{3} \\ &= i\Bigg\{\sum_{w=1}^{W}\sum_{u=1}^{w-1} -h_{w,1010}h_{u,0120}e^{i[\Delta\phi_{u,x}^{(s)}+\Delta\phi_{u,y}^{(s)}-\Delta\phi_{w,x}^{(s)}+2\Delta\phi_{w,y}^{(s)}]} + h_{w,0110}h_{u,1020}e^{i[-\Delta\phi_{u,x}^{(s)}+\Delta\phi_{u,y}^{(s)}+\Delta\phi_{w,x}^{(s)}+2\Delta\phi_{w,y}^{(s)}]} \\ &\quad - h_{w,1020}h_{u,0110}e^{i[\Delta\phi_{u,x}^{(s)}+2\Delta\phi_{u,y}^{(s)}-\Delta\phi_{w,x}^{(s)}+\Delta\phi_{w,y}^{(s)}]} + h_{w,0120}h_{u,1010}e^{i[-\Delta\phi_{u,x}^{(s)}+2\Delta\phi_{u,y}^{(s)}+\Delta\phi_{w,x}^{(s)}+\Delta\phi_{w,y}^{(s)}]}\Bigg\}h_{y,+}^{3}.\end{aligned} \tag{A22}$$

The second step in evaluating Eq. (A18) is the computation of $[\tilde{H}^{(1)}, \frac{\tilde{H}^{(1)}}{I-R}]$. After some algebra the following relations are derived

$$\begin{aligned}\frac{1}{2}\left[\tilde{H}^{(1)}, \frac{\tilde{H}^{(1)}}{I-R}\right] &= i\sum_{w=1}^{W}\sum_{u=1}^{W}\Bigg\{\sum_{jklm}\sum_{pqrt} h_{w,jklm}h_{u,pqrt}\frac{e^{i[(p-q)\Delta\phi_{u,x}^{(s)}+(r-t)\Delta\phi_{u,y}^{(s)}+(j-k)\Delta\phi_{w,x}^{(s)}+(l-m)\Delta\phi_{w,y}^{(s)}]}}{1-e^{2\pi i[(p-q)Q_x+(r-t)Q_y]}} \\ &\quad \times [(jq-kp)h_{x,+}^{j+p-1}h_{x,-}^{k+q-1}h_{y,+}^{l+r}h_{y,-}^{m+t} + (lt-mr)h_{x,+}^{j+p}h_{x,-}^{k+q}h_{y,+}^{l+r-1}h_{y,-}^{m+t-1}]\Bigg\}, \\ \frac{1}{2}\left[\tilde{H}^{(1)}, \frac{\tilde{H}^{(1)}}{I-R}\right]_{abcd} &= i\{\hat{h}_{abcd}^{(2)}(s)\}h_{x,+}^{a}h_{x,-}^{b}h_{y,+}^{c}h_{y,-}^{d} \Rightarrow \begin{cases} j+p-1=a \\ k+q-1=b \\ l+r=c \\ m+t=d \end{cases} \text{ or } \begin{cases} j+p=a \\ k+q=b \\ l+r-1=c \\ m+t-1=d \end{cases}.\end{aligned} \tag{A23}$$

The above expression is similar to the one of Eq. (A19) with two notable differences. Both summations here extend over the total number of magnets W, whereas the two are nested in Eq. (A19). The exponential term is now scaled by the rotational term $I-R$. However, the same selection rules of Eq. (A20) apply. It is worthwhile to mention that the more general case $[\tilde{H}^{(1)\ddagger}, \frac{\tilde{H}^{(1)\ddagger}}{I-R}]^{\ddagger}$ is retrieved by requesting that only those terms with $j \neq k$, $l \neq m$, $p \neq q$, and $r \neq t$ are included in the summations.

The explicit expression for the 0030 example, after applying the same selection rules of Eq. (A21), reads

$$\frac{1}{2}\left[\tilde{H}^{(1)},\frac{\tilde{H}^{(1)}}{I-R}\right]_{0030}(s) = i\{\hat{h}_{0030}(s)\}h_{y,+}^3$$
$$= i\left\{\sum_{w=1}^{W}\sum_{u=1}^{W} -h_{w,1010}h_{u,0120}\frac{e^{i[\Delta\phi_{u,x}^{(s)}+\Delta\phi_{u,y}^{(s)}-\Delta\phi_{w,x}^{(s)}+2\Delta\phi_{w,y}^{(s)}]}}{1-e^{2\pi i[Q_x+Q_y]}} + h_{w,0110}h_{u,1020}\frac{e^{i[-\Delta\phi_{u,x}^{(s)}+\Delta\phi_{u,y}^{(s)}+\Delta\phi_{w,x}^{(s)}+2\Delta\phi_{w,y}^{(s)}]}}{1-e^{2\pi i[-Q_x+Q_y]}}\right.$$
$$\left. - h_{w,1020}h_{u,0110}\frac{e^{i[\Delta\phi_{u,x}^{(s)}+2\Delta\phi_{u,y}^{(s)}-\Delta\phi_{w,x}^{(s)}+\Delta\phi_{w,y}^{(s)}]}}{1-e^{2\pi i[Q_x+2Q_y]}} + h_{w,0120}h_{u,1010}\frac{e^{i[-\Delta\phi_{u,x}^{(s)}+2\Delta\phi_{u,y}^{(s)}+\Delta\phi_{w,x}^{(s)}+\Delta\phi_{w,y}^{(s)}]}}{1-e^{2\pi i[-Q_x+2Q_y]}}\right\}h_{y,+}^3. \quad \text{(A24)}$$

The example is completed by writing the analytic expression for f_{0030} up to the second order

$$f_{0030} = f_{0030}^{(1)} + f_{0030}^{(2)} = \frac{1}{1-e^{2\pi i(3Q_y)}} \times\left\{\sum_{w=1}^{W} h_{w,0030}e^{i3\Delta\phi_{w,y}^{(s)}} + i\tilde{h}_{0030}^{(2)}(s) + i\hat{h}_{0030}(s)\right\}, \quad \text{(A25)}$$

where $\tilde{h}_{0030}^{(2)}(s)$ and $\hat{h}_{0030}(s)$ are excited by skew quadrupoles (via h_{1010} and h_{0110}) and normal sextupoles (via h_{1020} and h_{0120}), see Eqs. (A22) and (A24), while the first term in the r.h.s. is excited by either skew sextupoles, if any, or tilted normal sextupoles through h_{0030} and Eq. (A12). The Hamiltonian coefficients (h_{0030}, h_{1010}, and similar) may be computed from the magnet strengths and the C-S parameters via Eq. (A3). The same computation may be carried out for any other RDTs in the same way.

The last missing step is to include second-order terms in the change of coordinates of Eqs. (A13) and (A14). In analogy with the previous approach, the function F is split in its first- an second-order parts

$$\vec{h}(s,N) = e^{:F:}\vec{\zeta} = \vec{\zeta} + [F^{(1)}+F^{(2)},\vec{\zeta}] + \frac{1}{2}[F^{(1)}+F^{(2)},[F^{(1)}+F^{(2)},\vec{\zeta}]] + O(3^{\text{rd}})$$
$$= \vec{\zeta} + [F^{(1)}+F^{(2)},\vec{\zeta}] + \frac{1}{2}[F^{(1)},[F^{(1)},\vec{\zeta}]] + O(3^{\text{rd}}). \quad \text{(A26)}$$

The result is

$$h_{x,-}(s,N) = \zeta_{x,-} - 2i\sum_{abcd} a[f_{abcd}^{(1)}+f_{abcd}^{(2)}]\zeta_{x,+}^{a-1}\zeta_{x,-}^{b}\zeta_{y,+}^{c}\zeta_{y,-}^{d}$$
$$- 2\sum_{jklm}\sum_{pqrt} pf_{jklm}^{(1)}f_{pqrt}^{(1)}\{\zeta_{x,+}^{j+p-2}\zeta_{x,-}^{k+q-1}\zeta_{y,+}^{l+r}\zeta_{y,-}^{m+t} + (lt-mr)\zeta_{x,+}^{j+p-1}\zeta_{x,-}^{k+q}\zeta_{y,+}^{l+r-1}\zeta_{y,-}^{m+t-1}\}, \quad \text{(A27)}$$

$$h_{y,-}(s,N) = \zeta_{y,-} - 2i\sum_{abcd} c[f_{abcd}^{(1)}+f_{abcd}^{(2)}]\zeta_{x,+}^{a}\zeta_{x,-}^{b}\zeta_{y,+}^{c-1}\zeta_{y,-}^{d}$$
$$- 2\sum_{jklm}\sum_{pqrt} rf_{jklm}^{(1)}f_{pqrt}^{(1)}\{(jq-kp)\zeta_{x,+}^{j+p-1}\zeta_{x,-}^{k+q-1}\zeta_{y,+}^{l+r-1}\zeta_{y,-}^{m+t} + [lt-m(r-1)]\zeta_{x,+}^{j+p}\zeta_{x,-}^{k+q}\zeta_{y,+}^{l+r-2}\zeta_{y,-}^{m+t-1}\}. \quad \text{(A28)}$$

If second-order terms may be neglected, Eqs. (A15) and (A16) are retrieved. The above equations show how second-order terms prevent the direct measurement of the RDTs $f_{jklm} = f_{jklm}^{(1)} + f_{jklm}^{(2)}$ from the secondary spectral lines (harmonics in the first summation). Among the terms in the second double summation, in fact, there will be always some harmonics overlapping those of the first summation. An example may again help to clarify this point. Let us select in Eq. (A28) those terms proportional to $\zeta_{y,+}^2$, i.e., those exciting the spectral line $V_h(0,-2)$ (of the complex C-S variable $h_{y,-} = \tilde{y} - i\tilde{p}_y$). The first sum selects the index 0030, while in the second double summation only those index satisfying the following conditions shall be kept

$$\begin{cases} j+p-1=0 \\ k+q-1=0 \\ l+r-1=2 \\ m+t=0 \end{cases} \quad \text{or} \quad \begin{cases} j+p=0 \\ k+q=0 \\ l+r-2=2 \\ m+t-1=0 \end{cases}, \quad \text{(A29)}$$

resulting in

$$V_h(0,-2) = -6i\left\{ f^{(1)}_{0030} + f^{(2)}_{0030} - \frac{i}{3}[f^{(1)}_{1010}f^{(1)}_{0120} - f^{(1)*}_{1001}f^{(1)}_{1020} + 2f^{(1)}_{0020}f^{(1)}_{0021} - 6f^{(1)}_{0030}f^{(1)}_{0011}]\right\}\zeta^2_{y,+}. \quad \text{(A30)}$$

Assuming than no physical skew sextupoles exist, first-order skew sextupole RDTs $f^{(1)}_{0030}$ and $f^{(1)}_{0021}$ are generated by small tilts of normal sextupoles. Since focusing errors are assumed to be already small, the products $f^{(1)}_{0020}f^{(1)}_{0021}$ and $f^{(1)}_{0030}f^{(1)}_{0011}$ are negligible compared to the products $f^{(1)}_{1010}f^{(1)}_{0120}$ and $f^{(1)*}_{1001}f^{(1)}_{1020}$, both generated by the low coupling and the large sextupole RDTs. By making use of Eq. (A25), the observable RDT (ORDT) g_{0030} is

$$\begin{aligned} V_h(0,-2) &= -6i\{g_{0030}\}\zeta^2_{y,+} \\ &= -6i\left\{ f^{(1)}_{0030} + i\frac{\tilde{h}^{(2)}_{0030} + \hat{h}_{0030}}{1 - e^{2\pi i(3Q_y)}} \right. \\ &\quad \left. - \frac{i}{3}[f^{(1)}_{1010}f^{(1)}_{0120} - f^{(1)*}_{1001}f^{(1)}_{1020}]\right\}\zeta^2_{y,+}. \end{aligned} \quad \text{(A31)}$$

This example shows how the equivalence between the RDTs computed from the lattice and those either measured or evaluated from turn-by-turn data breaks down when second-order terms are to be included. In Table IV of Ref. [7] by using the spectral line $V_h(0,-2)$ to infer f_{0030} and hence the sextupole tilts may under- or overestimate the reality, since part of $V_h(0,-2)$ is also excited by second-order terms uncorrelated to the sextupole tilts.

APPENDIX B: QUADRUPOLE ERRORS AND TUNE LINE AMPLITUDE

In Table I (easier) first-order RDTs f_{jklm} for skew quadrupole and normal sextupole spectral lines are used, while for skew sextupoles (more complex) second-order ORDTs g_{jklm} are invoked. The latter are also used in Table VIII for normal octupoles. In this section motivations and conditions for such a choice are provided. It will be shown how this is related to the removal of RDTs generated by focusing errors when using the modulated β functions (i.e., computed from a lattice including quadrupole errors) rather than those of the ideal lattice.

Parenthetically, a novel procedure for using single-BPM turn-by-turn data to measure the β functions is described, which is complementary to the traditional approach based on the direct measurement of the phase advance between two consecutive BPMs [30]. The latter is independent on calibration errors, but requires a perfect synchronization among the BPMs. The proposed scheme, on the contrary, necessitates well-calibrated monitors but does not need any synchronization, as for the nonlinear analysis of Table I.

If focusing errors δK_1 are not included in the model, they generate the following RDTs

$$f_{2000} = \frac{\sum_w^W \delta K_{w,1}\beta_x^w e^{2i\Delta\phi_{w,x}}}{8(1 - e^{4\pi i Q_x})}, \quad \text{(B1)}$$

$$f_{0020} = \frac{\sum_w^W \delta K_{w,1}\beta_y^w e^{2i\Delta\phi_{w,y}}}{8(1 - e^{4\pi i Q_y})}. \quad \text{(B2)}$$

Provided that betatron coupling is sufficiently weak, i.e., that $2\mathcal{P} = \sqrt{-|2f_{1001}|^2 + |2f_{1010}|^2}$ of Ref. [21] is negligible compared to f_{2000}, the tune line amplitude of $\tilde{x} = x/\sqrt{\beta_x}$ is affected by the RDTs according to

$$\begin{aligned} |H(1,0)| = \frac{\sqrt{2I_x}}{2}\{1 + 2\sinh(4|f_{2000}|) \\ \times [\sinh(4|f_{2000}|) + \cosh(4|f_{2000}|)\sin q_{2000}]\}^{1/2}, \end{aligned} \quad \text{(B3)}$$

In Ref. [12] it is shown how by replacing the ideal β_x in the definition of $\tilde{x}$ with

$$\begin{aligned} \beta_{x1} = \beta_x\{1 + 2\sinh(4|f_{2000}|)[\sinh(4|f_{2000}|) \\ + \cosh(4|f_{2000}|)\sin q_{2000}]\} \end{aligned} \quad \text{(B4)}$$

a RDT-independent tune line, $|H(1,0)| = \sqrt{2I_x}/2$ is retrieved. Equivalent relations apply in the vertical plane after replacing f_{2000} with f_{0020}. Equation (B4) provides an analytical expression for the horizontal beta-beating introduced by quadrupole errors:

$$\begin{aligned} \frac{\Delta\beta_x}{\beta_x} = 2\sinh(4|f_{2000}|)[\sinh(4|f_{2000}|) \\ + \cosh(4|f_{2000}|)\sin q_{2000}]. \end{aligned} \quad \text{(B5)}$$

The same algebra applied to the vertical plane leads to

$$\begin{aligned} \frac{\Delta\beta_y}{\beta_y} = 2\sinh(4|f_{0020}|)[\sinh(4|f_{0020}|) \\ + \cosh(4|f_{0020}|)\sin q_{0020}]. \end{aligned} \quad \text{(B6)}$$

In Fig. 19 a comparison between the beta-beating as computed by MADX and by Eqs. (B5) and (B6) is shown. The agreement is remarkable.

In practice then, the perturbations introduced by the focusing error RDTs f_{2000} and f_{0020} of Eqs. (B1) and (B2) may be *absorbed* by replacing the ideal C-S parameters $\beta_{x,y}$ and $\Delta\phi_{x,y}$ with the modulated ones $\beta_{x1,y1}$ and $\Delta\phi_{x1,y1}$. By doing so, the new Courant-Snyder coordinates will no longer show quadrupole errors, and the beta-beat RDTs vanish, i.e.,

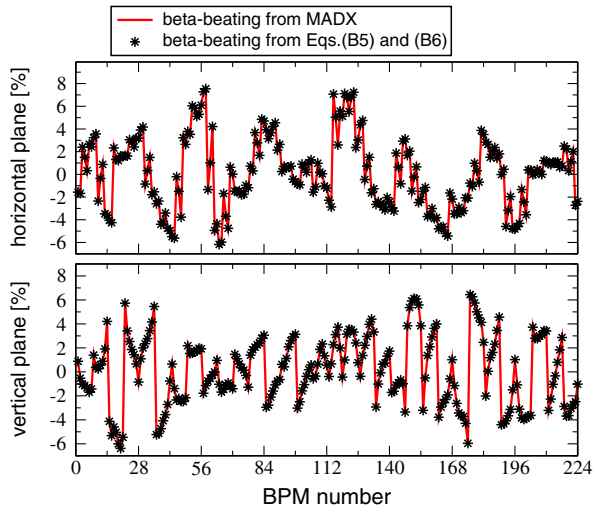

FIG. 19. Comparison between the beta-beating computed by MADX after loading an error model constructed from an ORM measurement in the ESRF storage ring (red) and that evaluated from Eqs. (B5) and (B6) (black stars).

$$f_{2000}(\beta_x, \Delta\phi_x) \neq 0 \quad \text{but} \quad f_{2000}(\beta_{x1}, \Delta\phi_{x1}) \equiv 0, \tag{B7}$$

$$f_{0020}(\beta_y, \Delta\phi_y) \neq 0 \quad \text{but} \quad f_{0020}(\beta_{x1}, \Delta\phi_{x1}) \equiv 0. \tag{B8}$$

Physically this corresponds to the fact that not including focusing errors in the computation of the C-S parameters results in *mismatched* functions and a phase space topology (ellipses) dependent on the longitudinal position along the ring (through the s-dependent beta-beating RDTs f_{2000} and f_{0020}). When, instead, the C-S parameters used to compute the C-S coordinates properly account for all normal quadrupole forces, the corresponding phase space topology becomes invariant along the ring (and circular).

If the number of oscillations of f_{2000} and f_{0020} along the ring is sufficiently large and the number of BPM is enough to cover uniformly the path, by averaging the tune line amplitudes among all BPMs, the oscillating term cancels out and the invariant may be retrieved:

$$\frac{\sqrt{2I_x}}{2} \simeq \frac{1}{N}\sum_{n=1}^{N} |H(1,0)|_n, \qquad \frac{\sqrt{2I_y}}{2} \simeq \frac{1}{N}\sum_{n=1}^{N} |V(0,1)|_n, \tag{B9}$$

where N is the number of available BPMs (not necessarily synchronized over the same turns and/or bunches) and $|H(1,0)|_n$ are the tune line amplitudes measured at the different monitors. More intriguingly, the same single-BPM turn-by-turn data may be post-processed to extract the true β function at its location, since

$$\beta_{x1,n} = \left(\frac{|H(1,0)|_n}{\langle |H(1,0)| \rangle}\right)^2 \beta_{x,n}, \tag{B10}$$

$$\beta_{y1,n} = \left(\frac{|V(0,1)|_n}{\langle |V(0,1)| \rangle}\right)^2 \beta_{y,n}. \tag{B11}$$

The use of the C-S parameters that already include focusing errors in evaluating the first-order RDTs of Table III not only will correctly account for the modulation introduced by the β functions, but has a tremendous impact in simplifying the second-order analysis of coupling and normal sextupole RDTs of Tables XII and XIII, respectively: The first-order beta-beat RDTs being all zero (as well as the corresponding Hamiltonian coefficients), second-order ORDTs g_{jklm} are equivalent to the first-order RDTs $f^{(1)}_{jklm}$. For this reason in Table I the latter are used in the entries corresponding to skew quadrupoles and normal sextupoles and no beta-beat RDT is reported in the tune lines. Second-order ORDTs g_{jklm} are instead used for the skew sextupolelike entries because they are generated by nonzero coupling and normal sextupole RDTs.

Focusing errors hence, if not included in the lattice model, modulate the tune line amplitudes and thus the β functions. The modulation is independent on the initial conditions (action and phase). Another, more complex, amplitude dependent modulation is introduced at the second order by normal sextupoles, requiring a careful preliminary analysis in order to make it negligible. The tune lines may be extracted from Eqs. (A27) and (A28) and include all terms proportional to $\zeta_{x,-}$ and $\zeta_{y,-}$ in the horizontal and vertical planes, respectively. In Ref. [12] it is shown that

$$H(1,0) = \{1 + T_{Hx}|\zeta_x|^2 + T_{Hy}|\zeta_y|^2\}\zeta_{x,-}, \tag{B12}$$

$$V(0,1) = \{1 + T_{Vx}|\zeta_x|^2 + T_{Vy}|\zeta_y|^2\}\zeta_{y,-}, \tag{B13}$$

where $T_{Hx,Hy}$ and $T_{Vx,Vy}$ vary along the ring and are quadratic functions of the first-order normal sextupoles RDTs ($f^{(1)}_{3000}, f^{(1)}_{1002}$, and similar). Equations (B12) and (B13) reveal also the nonlinear coupling introduced by sextupoles which makes the tune line amplitude in one plane dependent on the action $|\zeta|$ of the other. If not negligible, this nonlinear modulation may corrupt the evaluation of the invariants $(2I_{x,y})$ from the tune line amplitudes and hence the overall analysis discussed here, which is based on the formulas of Table II.

Given a certain sextupole setting, $T_{Hx,Hy}$ and $T_{Vx,Vy}$ are fixed. It is then of interest to estimate the largest beam oscillation amplitude that keeps the modulation below a tolerable level. To this end, preliminary single-particle tracking simulations at different initial conditions x_0 and y_0 (i.e., amplitudes) may be carried out. By storing the particle positions at all BPMs and performing the FFT of the Courant-Snyder coordinates $\tilde{x}$ and $\tilde{y}$, the tune line amplitudes may be plotted along the ring and their modulation evaluated against x_0 and y_0. In Fig. 20 an

TABLE XII. List and definition of second-order ORDTs g_{jklm} from the skew quadrupolelike secondary spectral lines of the complex C-S signals $h_{x,-} = \tilde{x} - i\tilde{p}_x$ ($h_{y,-} = \tilde{y} - i\tilde{p}_y$). First-order coupling RDTs $f^{(1)}_{1001}$ and $f^{(1)}_{1010}$ are those of Table III, derived from Eqs. (A12) and (A3). The second-order Hamiltonian terms $\tilde{h}^{(2)}_{jklm}$ and $\hat{h}_{jklm}$ are to be computed from Eqs. (A20) and (A23). Beta-beat RDTs $f^{(1)}_{2000}$ and $f^{(1)}_{0020}$ are defined in Eqs (B1) and (B2). If C-S parameters are evaluated from the linear lattice model with quadrupole errors included the second-order contributions vanish, i.e., $g_{jklm} = f^{(1)}_{jklm}$, as discussed in Appendix B.

h spectral line	$\{g_{jklm}\}$	Magnetic term
$H_h(0,1) = -2i\{g_{1001}\}\zeta_{y,-}$	$\left\{f^{(1)}_{1001} + i\frac{\tilde{h}^{(2)}_{1001} + \hat{h}_{1001}}{1 - e^{2\pi i(Q_x - Q_y)}} + i\left[2f^{(1)*}_{0020}f^{(1)}_{1010} + 2f^{(1)}_{2000}f^{(1)*}_{1010}\right]\right\}$	xy
$H_h(0,-1) = -2i\{g_{1010,H}\}\zeta_{y,+}$	$\left\{f^{(1)}_{1010} + i\frac{\tilde{h}^{(2)}_{1010} + \hat{h}_{1010}}{1 - e^{2\pi i(Q_x + Q_y)}} - i\left[2f^{(1)}_{0020}f^{(1)}_{1001} - 2f^{(1)}_{2000}f^{(1)*}_{1001}\right]\right\}$	xy
$V_h(1,0) = -2i\{g_{0110}\}\zeta_{x,-}$	$\left\{f^{(1)}_{0110} + i\frac{\tilde{h}^{(2)}_{0110} + \hat{h}_{0110}}{1 - e^{-2\pi i(Q_x - Q_y)}} + i\left[2f^{(1)}_{0020}f^{(1)*}_{1010} + 2f^{(1)*}_{2000}f^{(1)}_{1010}\right]\right\}$	xy
$V_h(-1,0) = -2i\{g_{1010,V}\}\zeta_{x,+}$	$\left\{f^{(1)}_{1010} + i\frac{\tilde{h}^{(2)}_{1010} + \hat{h}_{1010}}{1 - e^{2\pi i(Q_x + Q_y)}} + i\left[2f^{(1)}_{0020}f^{(1)}_{1001} - 2f^{(1)}_{2000}f^{(1)*}_{1001}\right]\right\}$	xy

example with betatron oscillations of $x_0 = 10$ mm and $y_0 = 2.2$ mm (large values by ESRF standards) is shown. Focusing errors are included in the model when computing the β functions and the residual modulation of about 3% is generated exclusively by sextupole RDTs. Results from a more complete scan of the ESRF storage ring are reported in Table XVI. They suggest to limit the transverse oscillation to $x_0 \simeq 3.5$ mm and $y_0 \simeq 1$ mm, corresponding to

TABLE XIII. List and definition of second-order ORDTs g_{jklm} from the normal sextupolelike secondary spectral lines of the complex C-S signals $h_{x,-} = \tilde{x} - i\tilde{p}_x$ ($h_{y,-} = \tilde{y} - i\tilde{p}_y$). First-order sextupolar RDTs ($f^{(1)}_{3000}$, $f^{(1)}_{1200}$, and similar) are those of Table III, derived from Eqs. (A12) and (A3). The second-order Hamiltonian terms $\tilde{h}^{(2)}_{jklm}$ and $\hat{h}_{jklm}$ are to be computed from Eqs. (A20) and (A23). Beta-beat RDTs $f^{(1)}_{2000}$ and $f^{(1)}_{0020}$ are defined in Eqs. (B1) and (B2). If C-S parameters are evaluated from the linear lattice model with quadrupole errors included, the second-order contributions vanish, i.e., $g_{jklm} = f^{(1)}_{jklm}$, as discussed in Appendix B. Products between skew sextupole and coupling RDTs have been excluded: It is indeed assumed that no physical strong skew sextupole is powered and that first-order skew sextupole RDTs are generated by small sextupole tilts. In Eqs. (A27) and (A28) skew sextupole first-order RDTs enter always multiplied by the already-small first-order coupling RDTs, hence making these products negligible.

h spectral line	$\{g_{jklm}\}$	Magnetic term
$H_h(-2,0) = -6i\{g_{3000}\}\zeta^2_{x,+}$	$\left\{f^{(1)}_{3000} + i\frac{\tilde{h}^{(2)}_{3000} + \hat{h}_{3000}}{1 - e^{2\pi i(3Q_x)}} - \frac{i}{3}\left[2f^{(1)}_{2000}f^{(1)*}_{1200}\right]\right\}$	x^3
$H_h(+2,0) = -2i\{g_{1200}\}\zeta^2_{x,-}$	$\left\{f^{(1)}_{1200} + i\frac{\tilde{h}^{(2)}_{1200} + \hat{h}_{1200}}{1 - e^{2\pi i(-Q_x)}} + i\left[4f^{(1)*}_{2000}f^{(1)*}_{1200} + 6f^{(1)}_{2000}f^{(1)*}_{3000}\right]\right\}$	x^3
$H_h(0,-2) = -2i\{g_{1020,H}\}\zeta^2_{y,+}$	$\left\{f^{(1)}_{1020} + i\frac{\tilde{h}^{(2)}_{1020} + \hat{h}_{1020}}{1 - e^{2\pi i(Q_x + 2Q_y)}} + i\left[2f^{(1)}_{2000}f^{(1)}_{0120} - 2f^{(1)}_{0020}f^{(1)*}_{0111}\right]\right\}$	xy^2
$H_h(0,+2) = -2i\{g_{1002}\}\zeta^2_{y,-}$	$\left\{f^{(1)}_{1002} + i\frac{\tilde{h}^{(2)}_{1002} + \hat{h}_{1002}}{1 - e^{2\pi i(Q_x - 2Q_y)}} + i\left[2f^{(1)*}_{0020}f^{(1)*}_{0111} + 2f^{(1)}_{2000}f^{(1)*}_{1020}\right]\right\}$	xy^2
$V_h(+1,+1) = -2i\{g_{0111}\}\zeta_{x,-}\zeta_{y,-}$	$\left\{f^{(1)}_{0111} + i\frac{\tilde{h}^{(2)}_{0111} + \hat{h}_{0111}}{1 - e^{2\pi i(-Q_x)}} + i\left[4f^{(1)*}_{0020}f^{(1)}_{0120} + 4f^{(1)}_{0020}f^{(1)*}_{1020} + 2f^{(1)}_{2000}f^{(1)*}_{0111}\right]\right\}$	xy^2
$V_h(-1,-1) = -4i\{g_{1020,V}\}\zeta_{x,+}\zeta_{y,+}$	$\left\{f^{(1)}_{1020} + i\frac{\tilde{h}^{(2)}_{1020} + \hat{h}_{1020}}{1 - e^{2\pi i(Q_x + 2Q_y)}} - i\left[2f^{(1)}_{2000}f^{(1)}_{0120}\right]\right\}$	xy^2
$V_h(+1,-1) = -4i\{g_{0120}\}\zeta_{x,-}\zeta_{y,+}$	$\left\{f^{(1)}_{0120} + i\frac{\tilde{h}^{(2)}_{0120} + \hat{h}_{0120}}{1 - e^{2\pi i(-Q_x + 2Q_y)}} + i\left[2f^{(1)*}_{2000}f^{(1)}_{1020}\right]\right\}$	xy^2
$V_h(-1,+1) = -2i\{g_{1011}\}\zeta_{x,+}\zeta_{y,-}$	$\left\{f^{(1)}_{1011} + i\frac{\tilde{h}^{(2)}_{1011} + \hat{h}_{1011}}{1 - e^{2\pi i(Q_x)}} + i\left[4f^{(1)*}_{0020}f^{(1)}_{1020} + 4f^{(1)}_{0020}f^{(1)*}_{0120} - 2f^{(1)}_{2000}f^{(1)}_{0111}\right]\right\}$	xy^2

TABLE XIV. List and definition of second-order ORDTs g_{jklm} from the skew sextupolelike secondary spectral lines of the complex C-S signals $h_{x,-} = \tilde{x} - i\tilde{p}_x$ ($h_{y,-} = \tilde{y} - i\tilde{p}_y$). First-order sextupolar RDTs ($f^{(1)}_{3000}$, $f^{(1)}_{1200}$, and similar) are those of Table III, derived from Eqs. (A12) and (A3). The second-order Hamiltonian terms $\tilde{h}^{(2)}_{jklm}$ and $\hat{h}_{jklm}$ are to be computed from Eqs. (A20) and (A23). ORDTs no longer have two RDTs properties: $g_{jklm} \neq g^*_{kjml}$ and $g_{jklm,H} \neq g_{jklm,V}$. Products between skew sextupole and beta-beat RDTs have been excluded: It is indeed assumed that no physical strong skew sextupole is powered and that first-order skew sextupole RDTs are generated by small sextupole tilts. In Eqs. (A27) and (A28) skew sextupole first-order RDTs enter always multiplied by the already-small beta-beat first-order RDTs, hence making these products negligible. See the 0030 example in the main text.

h spectral line	$\{g_{jklm}\}$	Magnetic term
$V_h(0,-2) = -6i\{g_{0030}\}\zeta^2_{y,+}$	$\left\{f^{(1)}_{0030} + i\frac{\tilde{h}^{(2)}_{0030} + \hat{h}_{0030}}{1 - e^{2\pi i(3Q_y)}} - \frac{i}{3}\left[f^{(1)}_{1010}f^{(1)}_{0120} - f^{(1)*}_{1001}f^{(1)}_{1020}\right]\right\}$	y^3
$V_h(0,+2) = -2i\{g_{0012}\}\zeta^2_{y,-}$	$\left\{f^{(1)}_{0012} + i\frac{\tilde{h}^{(2)}_{0012} + \hat{h}_{0012}}{1 - e^{2\pi i(-Q_y)}} - i\left[f^{(1)}_{1001}f^{(1)}_{0111} - f^{(1)*}_{1010}f^{(1)*}_{0111} + f^{(1)*}_{1001}f^{(1)*}_{0120} - f^{(1)}_{1010}f^{(1)*}_{1020}\right]\right\}$	y^3
$V_h(+2,0) = -2i\{g_{0210}\}\zeta^2_{x,-}$	$\left\{f^{(1)}_{0210} + i\frac{\tilde{h}^{(2)}_{0210} + \hat{h}_{0210}}{1 - e^{2\pi i(-2Q_x+Q_y)}} - i\left[f^{(1)*}_{1001}(f^{(1)}_{0111} + f^{(1)}_{1200}) - 2f^{(1)*}_{1010}f^{(1)}_{0120} - 3f^{(1)}_{1010}f^{(1)*}_{3000}\right]\right\}$	x^2y
$V_h(-2,0) = -2i\{g_{2010,V}\}\zeta^2_{x,+}$	$\left\{f^{(1)}_{2010} + i\frac{\tilde{h}^{(2)}_{2010} + \hat{h}_{2010}}{1 - e^{2\pi i(2Q_x+Q_y)}} - i\left[3f^{(1)*}_{1001}f^{(1)}_{3000} - 2f^{(1)}_{1001}f^{(1)}_{1020} + f^{(1)}_{1010}(f^{(1)*}_{0111} - f^{(1)*}_{1200})\right]\right\}$	x^2y
$H_h(+1,+1) = -2i\{g_{1101}\}\zeta_{x,-}\zeta_{y,-}$	$\left\{f^{(1)}_{1101} + i\frac{\tilde{h}^{(2)}_{1101} + \hat{h}_{1101}}{1 - e^{2\pi i(-Q_y)}} - i\left[2f^{(1)*}_{1001}f^{(1)*}_{0120} + f^{(1)}_{1001}(f^{(1)}_{0111} + 2f^{(1)}_{1200}) - 2f^{(1)}_{1010}f^{(1)*}_{1020} + f^{(1)*}_{1010}(-f^{(1)*}_{0111} - 2f^{(1)*}_{1200})\right]\right\}$	x^2y
$H_h(-1,-1) = -4i\{g_{2010,H}\}\zeta_{x,+}\zeta_{y,+}$	$\left\{f^{(1)}_{2010} + i\frac{\tilde{h}^{(2)}_{2010} + \hat{h}_{2010}}{1 - e^{2\pi i(2Q_x+Q_y)}} - \frac{i}{2}\left[2f^{(1)}_{1010}f^{(1)*}_{1200} - 6f^{(1)*}_{1001}f^{(1)}_{3000}\right]\right\}$	x^2y
$H_h(+1,-1) = -2i\{g_{1110}\}\zeta_{x,-}\zeta_{y,+}$	$\left\{f^{(1)}_{1110} + i\frac{\tilde{h}^{(2)}_{1110} + \hat{h}_{1110}}{1 - e^{2\pi i(Q_y)}} - i\left[2f^{(1)}_{1001}f^{(1)}_{0120} + f^{(1)}_{1010}(-f^{(1)}_{0111} + 2f^{(1)}_{1200}) - 2f^{(1)*}_{1010}f^{(1)}_{1020} + f^{(1)*}_{1001}(f^{(1)*}_{0111} - 2f^{(1)*}_{1200})\right]\right\}$	x^2y
$H_h(-1,+1) = -4i\{g_{2001}\}\zeta_{x,+}\zeta_{y,-}$	$\left\{f^{(1)}_{2001} + i\frac{\tilde{h}^{(2)}_{2001} + \hat{h}_{2001}}{1 - e^{2\pi i(2Q_x-Q_y)}} - \frac{i}{2}\left[2f^{(1)}_{1001}f^{(1)*}_{1200} - 6f^{(1)*}_{1010}f^{(1)}_{3000}\right]\right\}$	x^2y

$\sqrt{2I_x} \simeq \sqrt{2I_y} \simeq 3.1 \times 10^{-4}$ m$^{1/2}$ with relative variation of about 0.2%, well within the measurement statistical fluctuations of about 1%. Larger oscillations would induce a beneficial larger spectral resolution (higher ratio between sextupolar secondary lines and background noise), but also a larger modulation of the tune line amplitudes, which is detrimental for the correct evaluation of the invariants $2I_{x,y}$, hampering in turn the correct measurements of sextupolar RDTs.

As reported in Ref. [4], the spectral line $H_h(-1,0)$ of the complex C-S signals $\tilde{x} - i\tilde{p}_x$ receives a contribution from the normal octupole term x^4 via two ORDTs, g_{3100} and g_{2011}. It can be shown that

$$H_h(-1,0) = [3g_{3100}(2I_x)^{3/2} + 4g_{2011}(2I_x)^{1/2}(2I_y)] \times (-2i)e^{-i(2\pi Q_x N + \psi_{x0})}. \quad \text{(B14)}$$

This implies that, on top of the focusing errors not included in the model and second-order normal sextupole terms, the tune line $H(1,0)$ of the real C-S signal $\tilde{x}$ receives a contribution from octupolar terms, since $H(1,0) = 1/2[H_h(1,0) + H_h(-1,0)]$. Three problems arise at large excitation amplitude and or with large octupolar components in the lattice: (i) The tune phase is affected by octupolar terms and the linear lattice modeling discussed in Sec. IV B is corrupted; (ii) It is no longer possible to extract any linear combination of g_{3100} and g_{2011}, because of the different dependence on the action of the two terms, $\propto (2I_x)^{3/2}$ and $\propto (2I_x)^{1/2}(2I_y)$, respectively; (iii) The tune line amplitude is no longer equal to $(2I_x)^{1/2}$ and the computation of the other CRDTs from Tables II and IX are affected by an intrinsic error. Equivalent considerations apply for the vertical tune line, affected by the y^4 octupolar terms, g_{0013} and g_{1102}.

In conclusion, the turn-by-turn analysis of the nonlinear lattice model may be carried out and the formulas of Tables I and II applied provided that: (i) Focusing errors are correctly included in the model when computing the C-S

TABLE XV. List and definition of second-order ORDTs g_{jklm} from the normal octupolelike secondary spectral lines of the complex C-S signals $h_{x,-} = \tilde{x} - i\tilde{p}_x$ ($h_{y,-} = \tilde{y} - i\tilde{p}_y$). First-order sextupolar terms ($f^{(1)}_{3000}$, $f^{(1)}_{1200}$, and similar) are those of Table III, whereas first-order octupolar RDTs ($f^{(1)}_{4000}$, $f^{(1)}_{1300}$, ...) may be computed from Eqs. (A12) and (A3). The second-order Hamiltonian terms $\tilde{h}^{(2)}_{jklm}$ and $\hat{h}_{jklm}$ are to be computed from Eqs. (A20) and (A23). ORDTs have no longer two RDTs properties: $g_{jklm} \neq g^*_{kjml}$ and $g_{jklm,H} \neq g_{jklm,V}$. If quadrupole errors are included in the model when computing the C-S parameters, first-order quadrupolar RDTs vanish, i.e., $f^{(1)}_{2000} = f^{(1)}_{0020} = 0$.

h spectral line	$\{g_{jklm}\}$	Magnetic term
$H_h(-3,0) = -8i\{g_{4000}\}\zeta^3_{x,+}$	$\left\{f^{(1)}_{4000} + i\frac{\tilde{h}^{(2)}_{4000} + \hat{h}_{4000}}{1 - e^{2\pi i(4Q_x)}} - i\left[f^{(1)}_{2000}f^{(1)}_{3100}\right]\right\}$	x^4
$H_h(3,0) = -2i\{g_{1300}\}\zeta^3_{x,-}$	$\left\{f^{(1)}_{1300} + i\frac{\tilde{h}^{(2)}_{1300} + \hat{h}_{1300}}{1 - e^{2\pi i(-2Q_x)}} + i\left[6f^{(1)*}_{3000}f^{(1)*}_{1200} - 2f^{(1)2}_{1200} + 8f^{(1)}_{2000}f^{(1)}_{4000}\right]\right\}$	x^4
$H_h(-1,2) = -4i\{g_{2002}\}\zeta_{x,+}\zeta^2_{y,-}$	$\left\{f^{(1)}_{2002} + i\frac{\tilde{h}^{(2)}_{2002} + \hat{h}_{2002}}{1 - e^{2\pi i(2Q_x - 2Q_y)}} + i\left[3f^{(1)*}_{1020}f^{(1)}_{3000} - f^{(1)}_{1002}f^{(1)*}_{1200} + 2f^{(1)*}_{0020}f^{(1)}_{2011}\right]\right\}$	x^2y^2
$H_h(1,-2) = -2i\{g_{1120}\}\zeta_{x,-}\zeta^2_{y,+}$	$\left\{f^{(1)}_{1120} + i\frac{\tilde{h}^{(2)}_{1120} + \hat{h}_{1120}}{1 - e^{2\pi i(2Q_y)}} - 2i\left[f^{(1)}_{1020}(f^{(1)}_{1200} - f^{(1)}_{0111}) + f^{(1)}_{0120}(f^{(1)*}_{0111} - f^{(1)*}_{1200}) - 2(f^{(1)*}_{2000}f^{(1)}_{2020} + f^{(1)}_{2000}f^{(1)}_{0220})\right]\right\}$	x^2y^2
$H_h(1,2) = -2i\{g_{1102}\}\zeta_{x,-}\zeta^2_{y,-}$	$\left\{f^{(1)}_{1102} + i\frac{\tilde{h}^{(2)}_{1102} + \hat{h}_{1102}}{1 - e^{2\pi i(-2Q_y)}} - 2i\left[f^{(1)*}_{0120}(f^{(1)}_{1200} + f^{(1)}_{0111}) - f^{(1)*}_{1020}(f^{(1)*}_{0111} + f^{(1)*}_{1200}) - 2(f^{(1)*}_{2000}f^{(1)}_{2002} + f^{(1)}_{2000}f^{(1)}_{2020})\right]\right\}$	x^2y^2
$H_h(-1,-2) = -4i\{g_{2020,H}\}\zeta_{x,+}\zeta^2_{y,+}$	$\left\{f^{(1)}_{2020} + i\frac{\tilde{h}^{(2)}_{2020} + \hat{h}_{2020}}{1 - e^{2\pi i(2Q_x + 2Q_y)}} + i\left[3f^{(1)}_{0120}f^{(1)}_{3000} - f^{(1)}_{1020}f^{(1)*}_{1200} + 2f^{(1)}_{0020}f^{(1)}_{2011}\right]\right\}$	x^2y^2
$V_h(-2,-1) = -4i\{g_{2020,V}\}\zeta^2_{x,+}\zeta_{y,+}$	$\left\{f^{(1)}_{2020} + i\frac{\tilde{h}^{(2)}_{2020} + \hat{h}_{2020}}{1 - e^{2\pi i(2Q_x + 2Q_y)}} - i\left[3f^{(1)}_{0120}f^{(1)}_{3000} - f^{(1)}_{1020}f^{(1)*}_{1200} + 2f^{(1)}_{2000}f^{(1)}_{1120}\right]\right\}$	x^2y^2
$V_h(-2,1) = -2i\{g_{2011}\}\zeta^2_{x,+}\zeta_{y,-}$	$\left\{f^{(1)}_{2011} + i\frac{\tilde{h}^{(2)}_{2011} + \hat{h}_{2011}}{1 - e^{2\pi i(2Q_x)}} - i\left[3f^{(1)}_{3000}f^{(1)}_{0111} - f^{(1)*}_{1200}f^{(1)*}_{0111} - 4f^{(1)*}_{0120}f^{(1)}_{1020} + f^{(1)*2}_{0111} - 4(f^{(1)*}_{0020}f^{(1)}_{2020} + f^{(1)}_{0020}f^{(1)}_{2002})\right]\right\}$	x^2y^2
$V_h(2,-1) = -4i\{g_{0220}\}\zeta^2_{x,-}\zeta_{y,+}$	$\left\{f^{(1)}_{0220} + i\frac{\tilde{h}^{(2)}_{0220} + \hat{h}_{0220}}{1 - e^{2\pi i(-2Q_x + 2Q_y)}} + i\left[3f^{(1)*}_{3000}f^{(1)}_{1020} - f^{(1)}_{1200}f^{(1)}_{0120} + 2f^{(1)*}_{2000}f^{(1)}_{1120}\right]\right\}$	x^2y^2
$V_h(2,1) = -2i\{g_{0211}\}\zeta^2_{x,-}\zeta_{y,-}$	$\left\{f^{(1)}_{0211} + i\frac{\tilde{h}^{(2)}_{0211} + \hat{h}_{0211}}{1 - e^{2\pi i(-2Q_x)}} - i\left[f^{(1)}_{0111}(f^{(1)}_{1200} + f^{(1)}_{0111}) - 3f^{(1)*}_{3000}f^{(1)*}_{0111} - 4f^{(1)*}_{1020}f^{(1)}_{0120} - 4(f^{(1)}_{0020}f^{(1)}_{0202} + f^{(1)*}_{0020}f^{(1)}_{0220})\right]\right\}$	x^2y^2
$V_h(0,-3) = -8i\{g_{0040}\}\zeta^3_{y,+}$	$\left\{f^{(1)}_{0040} + i\frac{\tilde{h}^{(2)}_{0040} + \hat{h}_{0040}}{1 - e^{2\pi i(4Q_y)}} - i\left[f^{(1)}_{0020}f^{(1)*}_{0013}\right]\right\}$	y^4
$V_h(0,3) = -2i\{g_{0013}\}\zeta^3_{y,-}$	$\left\{f^{(1)}_{0013} + i\frac{\tilde{h}^{(2)}_{0013} + \hat{h}_{0013}}{1 - e^{2\pi i(-2Q_y)}} + i\left[f^{(1)*}_{1020}f^{(1)*}_{0111} + f^{(1)*}_{0120}f^{(1)}_{0111} - 8f^{(1)}_{0020}f^{(1)*}_{0040}\right]\right\}$	y^4

parameters to be used when evaluating the first-order RDTs of Table III and when normalizing the measured turn-by-turn data before performing the FFT, $\tilde{x} = x/\sqrt{\beta_x}$ and $\tilde{y} = y/\sqrt{\beta_y}$; (ii) The transverse beam excitation is conveniently chosen as a trade off between maximizing the spectral signal-to-noise ratio and minimizing the tune line modulation induced by sextupoles and octupoles. This will result in tune lines having the same amplitude along the ring ($|H(1,0)| \simeq \sqrt{2I_x}/2$ and $|V(0,1)| \simeq \sqrt{2I_y}/2$), in zero beta-beat RDTs, and hence in the possibility of using first-order RDTs for the analysis of normal sextupole errors.

APPENDIX C: COMBINED RDTS FRM SINGLE-BPM TURN-BY-TURN DATA

In this appendix the procedure for the evaluation of the single-BPM combined RDTs (CRDTs) of Tables I and VIII is outlined. As discussed in Appendix B it is assumed that quadrupole errors are included in the computation of the C-S parameters, and that transverse oscillations are sufficiently small to neglect the interference of sextupole and octupole RDTs on the tune lines. Equations (A27) and (A28) may be rewritten as

TABLE XVI. Dependence of tune line amplitudes mean value and rms modulation against initial conditions evaluated from single-particle tracking and FFT of the particle position recorded at the 224 BPMs in the ESRF storage ring. The sextupole setting is the same used in the experiments and focusing errors are included in the lattice model. The observed amplitude dependent modulation is due to second-order sextupole terms.

(x_0, y_0) (mm)	$(\lvert H(1,0)\rvert, \lvert V(0,1)\rvert)$ mean value $m^{1/2}$	$(\lvert H(1,0)\rvert, \lvert V(0,1)\rvert)$ rms modul. $m^{1/2}$	Relative modulation
(0.4, 0.1)	$(0.3, 0.3) \times 10^{-4}$	$(3.1, 2.7) \times 10^{-9}$	$\sim 10^{-4}$
(1.2, 0.5)	$(1.0, 1.4) \times 10^{-4}$	$(4.6, 5.0) \times 10^{-8}$	$< 10^{-3}$
(2.2, 0.5)	$(2.0, 1.4) \times 10^{-4}$	$(0.1, 0.1) \times 10^{-6}$	$< 10^{-3}$
(2.2, 0.7)	$(2.0, 2.0) \times 10^{-4}$	$(0.2, 0.2) \times 10^{-6}$	$\sim 0.1\%$
(2.8, 0.8)	$(2.6, 2.6) \times 10^{-4}$	$(0.4, 0.4) \times 10^{-6}$	$\sim 0.2\%$
(4.5, 0.8)	$(4.1, 2.6) \times 10^{-4}$	$(0.8, 0.9) \times 10^{-6}$	$\sim 0.3\%$
(4.4, 0.9)	$(4.1, 3.0) \times 10^{-4}$	$(0.9, 1.1) \times 10^{-6}$	$\sim 0.4\%$
(8.0, 2.0)	$(8.9, 6.9) \times 10^{-4}$	$(1.1, 1.5) \times 10^{-5}$	$\sim 2\%$

$$h_x(N) = \sqrt{2I_x} e^{i(2\pi Q_x N + \psi_{x0})} - 2i \sum_{jklm} j g_{jklm} (2I_x)^{\frac{j+k-1}{2}} (2I_y)^{\frac{l+m}{2}} e^{i[(1-j+k)(2\pi Q_x N + \psi_{x0}) + (m-l)(2\pi Q_y N + \psi_{y0})]}, \tag{C1}$$

and, equivalently for the vertical plane,

$$h_y(N) = \sqrt{2I_y} e^{i(2\pi Q_y N + \psi_{y0})} - 2i \sum_{jklm} l g_{jklm} (2I_x)^{\frac{j+k}{2}} (2I_y)^{\frac{l+m-1}{2}} e^{i[(k-j)(2\pi Q_x N + \psi_{x0}) + (1-l+m)(2\pi Q_y N + \psi_{y0})]}. \tag{C2}$$

g_{jklm} are the ORDT of Tables XII–XV, measurable at the location of a generic BPM. The four indices are selected according to the type of the magnetic elements exciting the RDTs and obey to the selection rules of Table XVII. The real parts of the above expressions read

$$\tilde{x}(N) = \frac{\sqrt{2I_x}}{2} [e^{i(2\pi Q_x N + \psi_{x0})} + \text{c.c}] + 2 \sum_{jklm} j (2I_x)^{\frac{j+k-1}{2}} (2I_y)^{\frac{l+m}{2}} \Im\{g_{jklm} e^{i[(1-j+k)(2\pi Q_x N + \psi_{x0}) + (m-l)(2\pi Q_y N + \psi_{y0})]}\}, \tag{C3}$$

$$\tilde{y}(N) = \frac{\sqrt{2I_y}}{2} [e^{i(2\pi Q_y N + \psi_{y0})} + \text{c.c}] + 2 \sum_{jklm} l (2I_x)^{\frac{j+k}{2}} (2I_y)^{\frac{l+m-1}{2}} \Im\{g_{jklm} e^{i[(k-j)(2\pi Q_x N + \psi_{x0}) + (1-l+m)(2\pi Q_y N + \psi_{y0})]}\}. \tag{C4}$$

In deriving the above equations, the relation $\Re\{iz\} = -\Im\{z\}$, valid for any complex number z, is used. $c.c.$ stands for complex conjugate. The following relations then apply

$$\begin{cases} (2I_x) = (2|H(1,0)|)^2 \\ \psi_{x0} = \arg\{H(1,0)\} \end{cases}, \quad \begin{cases} (2I_y) = (2|V(0,1)|)^2 \\ \psi_{y0} = arg\{V(0,1)\} \end{cases}. \tag{C5}$$

Let us start with coupling CRDTs. By replacing g_{jklm} with the first-order RDTs $f^{(1)}_{jklm}$ and selecting in Eq. (C3) those terms satisfying the conditions $j + k = 1$ and $m + l = 1$ the following harmonics are generated

$$\begin{aligned} &2\sqrt{2I_y} \Im\{f^{(1)}_{1001} e^{i(2\pi Q_y N + \psi_{y0})] } + f^{(1)}_{1010} e^{-i(2\pi Q_y N + \psi_{y0})]}\} \\ &= \frac{\sqrt{2I_y}}{i} [(f^{(1)}_{1001} - f^{(1)*}_{1010}) e^{i(2\pi Q_y N + \psi_{y0})} \\ &\quad - (f^{(1)*}_{1001} - f^{(1)}_{1010}) e^{-i(2\pi Q_y N + \psi_{y0})}] \\ &= \frac{\sqrt{2I_y}}{i} [F_{xy} e^{i(2\pi Q_y N + \psi_{y0})} - \text{c.c.}], \end{aligned} \tag{C6}$$

where

$$\begin{cases} |H(0,1)| = \sqrt{2I_y} |F_{xy}| \\ \arg\{H(0,1)\} = q_{F_{xy}} + \frac{3}{2}\pi + \psi_{y0} \end{cases} \Rightarrow \begin{cases} F_{xy} = f^{(1)}_{1001} - f^{(1)*}_{1010} \\ |F_{xy}| = |H(0,1)|/(2|V(0,1)|) \\ q_{F_{xy}} = \arg\{H(0,1)\} - \frac{3}{2}\pi - \arg\{V(0,1)\} \end{cases}, \tag{C7}$$

since both $(2I_y)$ and ψ_{y0} are measurable from the vertical tune line $V(0,1)$, via Eq. (C5). It shall be noticed that a choice must be made on the selection of the spectral line, since Eq. (C6) is real. F_{xy} may be inferred from either $H(0,1)$ or by its complex conjugate $H(0,-1)$: These two lines have equal amplitudes but opposite phases. The choice is made here to make use of the lines in the region [0,0.5] in tune units, assuming that both tunes $Q_{x,y}$ lie in that interval. With this assumption, $H(0,1)$ is used, while $H(0,-1)$ is rejected. If the tunes are in the region [0.5,1],

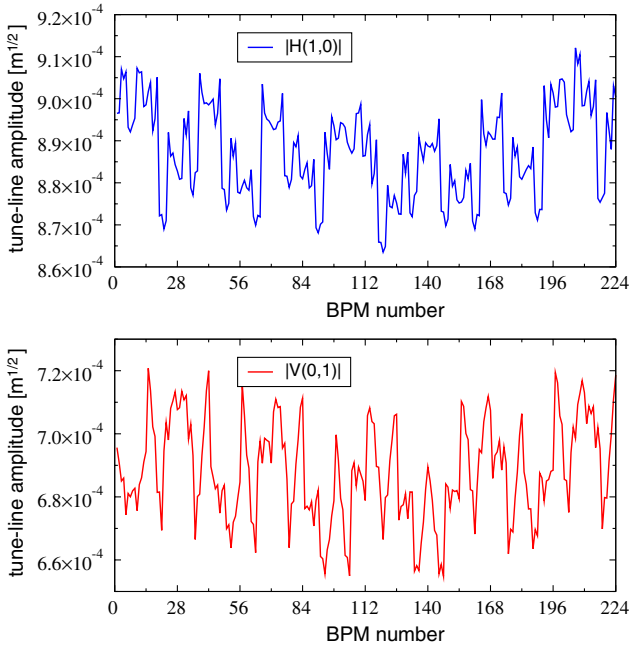

FIG. 20. Example of variation of the horizontal (top) and vertical (bottom) tune line amplitudes along the ESRF storage ring (224 BPMs, tracking simulations and FFT with initial conditions $x_0 = 8$ mm and $y_0 = 2.0$ mm, last row of Table XVI). Normal sextupoles induce a modulation in both planes of about 2%, which would be zero in their absence.

the opposite is true. This rule will apply to all secondary spectral lines discussed in this paper. The same algebra repeated for the vertical signal of Eq. (C4):

$$\begin{aligned} &2\sqrt{2I_x}\Im\{f^{(1)}_{0110}e^{i(2\pi Q_x N+\psi_{x0})]} + f^{(1)}_{1010}e^{-i(2\pi Q_x N+\psi_{x0})]}\} \\ &\quad = \frac{\sqrt{2I_x}}{i}\left[(f^{(1)}_{0110} - f^{(1)*}_{1010})e^{i(2\pi Q_x N+\psi_{x0})}\right. \\ &\quad\quad \left. - (f^{(1)*}_{0110} - f^{(1)}_{1010})e^{-i(2\pi Q_x N+\psi_{x0})}\right] \\ &\quad = \frac{\sqrt{2I_x}}{i}[F_{yx}e^{i(2\pi Q_x N+\psi_{x0})} - \text{c.c.}], \end{aligned} \tag{C8}$$

where

$$\begin{cases} |V(1,0)| = \sqrt{2I_x}|F_{yx}| \\ \arg\{V(1,0)\} = q_{F_{yx}} + \frac{3}{2}\pi + \psi_{x0} \end{cases}, \\ \Rightarrow \begin{cases} F_{yx} = f^{(1)}_{0110} - f^{(1)*}_{1010} \\ |F_{yx}| = |V(1,0)|/(2|H(1,0)|) \\ q_{F_{yx}} = \arg\{V(1,0)\} - \frac{3}{2}\pi - \arg\{H(1,0)\} \end{cases}. \tag{C9}$$

$(2I_x)$ and ψ_{x0} are replaced by the horizontal tune line $H(1,0)$, via Eq. (C5). Equations (C7) and (C9) prove the skew quadrupole entries in Tables I and II. Even though these two equations form a linear system, it is impossible to extract the two coupling RDTs from the two CRDTs, the system being degenerate. Nevertheless, the following relation applies

$$F_{xy0} = \Re\{F_{xy}\} - \Re\{F_{yx}\} \equiv 0. \tag{C10}$$

F_{xy0} may be then used to assess the reliability of the harmonic analysis, as far as coupling is concerned, in the same way F_0 of Eq. (7) does for the sextupolar analysis.

The same procedure may be applied for the normal sextupole spectral lines of Table I, again replacing the ORDTs g_{jklm} by the first-order RDTs $f^{(1)}_{jklm}$ in Eqs. (C3) and (C4). For skew sextupole and normal octupole spectral lines the ORDTs of Tables XIV and XV, respectively, shall be used. For more details, see Ref. [12].

TABLE XVII. Selection of index relative to the magnets.

Multipole kind	Magnetic term	Index relations
Normal quadrupole	x^2	$j+k=2\ m+l=0$
Normal quadrupole	y^2	$j+k=0\ m+l=2$
Skew quadrupole	xy	$j+k=1\ m+l=1$
Normal sextupole	x^3	$j+k=3\ m+l=0$
Normal sextupole	xy^2	$j+k=1\ m+l=2$
Skew sextupole	y^3	$j+k=0\ m+l=3$
Skew sextupole	x^2y	$j+k=2\ m+l=1$
Normal octupole	x^4	$j+k=4\ m+l=0$
Normal octupole	y^4	$j+k=0\ m+l=4$
Normal octupole	x^2y^2	$j+k=2\ m+l=2$

[1] D. D. Caussyn, M. Ball, B. Brabson, J. Collins, S. A. Crtis, V. Derenchuk, D. Duplantis, G. East, M. Ellison, T. Ellison, D. Friesel, B. Hamilton, W. P. jones, W. Lamble, S. Y. lee, D. Li, M. G. Minty, T. Sloan, G. Xu, A. W. Chao, K. Y. Ng, and S. Tepikian, Phys. Rev. A **46**, 7942 (1992).

[2] A. Bazzani, E. Todesco, G. Turchetti, and G. Servizi, Report No. CERN 94-02, 1994.

[3] É. Forest *et al.*, *Particle Accelerators* ***24****, 91 (1989).*

[4] R. Bartolini and F. Schmidt, *Particle Accelerators* ***59****, 93 (1998).*

[5] R. Tomás García, Ph.D. thesis, University of Valencia (Report No. CERN-THESIS-2003-010, 2003).

[6] A. Franchi, Ph.D. thesis, J.W. Goethe University (Report No. GSI DISS 2006-07, 2006).

[7] A. Franchi, R. Tomás García, and F. Schmidt, Phys. Rev. ST Accel. Beams **10**, 074001 (2007).

[8] J. S. Kolski, R. J. Macek, R. C. McCrady, and X. Pang, Phys. Rev. ST Accel. Beams **15**, 112802 (2012); X. Pang and S. Y. Lee, J. Appl. Phys. **106**, 074902 (2009); X. Pang, Ph.D. thesis, Indiana University, 2009.

[9] R. Bartolini, I. P. S. Martin, J. H. Rowland, P. Kuske, and F. Schmidt, Phys. Rev. ST Accel. Beams **11**, 104002 (2008).

[10] T. Bach, S. Gilardoni, M. Giovannozzi, C. Hernalsteens, A. Lachaize, G. Sterbini, R. Tomás, and R. Wasef, in *Proceedings of the 4th International Particle Accelerator Conference, IPAC-2013, Shanghai, China, 2013* (JACoW, Shanghai, China, 2013).
[11] G. Vanbavinckhove, M. Aiba, A. Nadji, L. Nadolski, R. Tomás, and M-A. Tordeux, in *Proceedings of the 23rd Particle Accelerator Conference, Vancouver, Canada, 2009* (IEEE, Piscataway, NJ, 2009).
[12] A. Franchi, L. Farvacque, F. Ewald, G. Le Bec, and K. B. Scheidt, arXiv:1402.1461.
[13] J. Laskar, C. Froeschlé, and A. Celletti, Physica D (Amsterdam) **56**, 253 (1992).
[14] R. Bartolini, A. Bazzani, M. Giovannozzi, W. Scandale, and E. Todesco, Report No. CERN SL/95-84 (AP), 1995.
[15] N. Minty and F. Zimmermann, *Measurement and Control of Charged Particle Beams* (Springer, Berlin, 2003).
[16] R. E. Meller, A. W. Chao, J. M. Pereson, S. G. Peggs, and M. Furman, Report No. SSC-N-360, 1987.
[17] B. K. Scheidt and F. Epaud, in *Proceedings of the 9th European Workshop on Beam Diagnostics and Instrumentation for Particle Accelerators DIPAC-2009, Basel, Switzerland, 2009* (JACoW, Basel, Switzerland, 2009), p. 50.
[18] A. Kosicek, in *Proceedings of the Beam Instrumentation Workshop BIW-2008, Lake Tahoe, 1581 USA, 2008* (JACoW, Lake Tahoe, USA, 2008), p. 186.
[19] R. Tomás, Phys. Rev. ST Accel. Beams **5**, 054001 (2002).
[20] S. White, E. Maclean, and R. Tomás, Phys. Rev. ST Accel. Beams **16**, 071002 (2013).
[21] A. Franchi, E. Métral, and R. Tomás García, Phys. Rev. ST Accel. Beams **10**, 064003 (2007).
[22] G. De Ninno and E. Todesco, Phys. Rev. E **55**, 2059 (1997).
[23] G. Ripken and F. Willeke, *Particle Accelerators **27**, 203 (1990)*.
[24] W. Herr and F. Schmidt, CERN AB Report No. CERN-AB-2004-027-ABP, 2004.
[25] A. Franchi, L. Farvacque, J. Chavanne, F. Ewald, B. Nash, K. Scheidt, and R. Tomás, Phys. Rev. ST Accel. Beams **14**, 034002 (2011).
[26] J. Jacob, Y. Papaphilippou, and A. Ropert, ESRF Report No. ESRF/MACH 04/60, 2004.
[27] M. Lieuvin, ESRF Report No. 730-91/ML-AP, 1991.
[28] J. Bengtsson and J. Irwin, SSC Report No. SSC-232, Berkeley, CA, 1990.
[29] A. Franchi, S. Gilardoni, and M. Giovannozzi, Phys. Rev. ST Accel. Beams **12**, 014001 (2009).
[30] P. Castro García, Ph.D. thesis, University of Valencia, (Report No. CERN-SL-96-070-BI, 1996).